cell of origin, the cell from which the tumor initiates, is often not known, or these cells are not available in sufficient quantities. Therefore—at least theoretically—all DNA methylation 'changes' found in tumor DNA may already preexist in the cell of origin. However, we argue that methylation of genes that promote the differentiation of neuroendocrine cells would be unlikely to occur in such cells as that would interfere with their normal differentiated state.

The SCLC patients investigated in this study showed a strong enrichment of tumor-specific methylation at homeobox genes (Supplementary Tables 15 and 16). Homeobox genes and other transcriptional regulators are important for developmental processes, having important roles in cellular identity, growth, differentiation and cellular interactions within the tissue environment. Given the results of our study, we developed a theory that disruptions in the early phase of these processes would increase the probability of the cell to become malignant, as this would lead to a pool of cells, which are aberrantly kept in a proliferation loop without a decision toward a specific cell fate. As already mentioned, it is thought that the cells of origin for SCLC are neuroendocrine cells, as shown in mice.[10,11] Given the fact that many of the tumor-specifically methylated targets we identified are important for cell fate decisions toward the neuronal lineage, it is intriguing to speculate that one way of shifting the balance toward the emergence of SCLC would be through the repression of key factors critical for differentiation of neuroendocrine cells. One potential way of aberrant shutdown of these critical factors would be by promoter-targeted methylation. Being freed of their normal developmental program by the absence or reduction of cell fate specification factors, some of these cells could acquire additional malignant traits, according to the 'hallmark' model defined by Hanahan and Weinberg.[39] This means that the observed hypermethylated regions are more probable to arise at an early stage of perturbed differentiation rather than during the later stages of tumorigenesis. Concerning other tumor-driving aberrant methylation events, which might increase the tumorigenic potential, it is interesting to note that we could rarely detect any promoter-specific methylation close to known tumor suppressor genes. Exceptions were tumor-specific methylation of *TCF21*,[40] which was detected downstream of the gene in the tumors but overlapping with the TSS in the cell lines and methylation of the promoter of the *RASSF1A* gene confirming earlier gene-specific studies.[17,18]

Another potential way of disrupting cell fate decisions is not by merely reducing the responsible factors but by altering the selectivity toward their genomic recognition sites by aberrant methylation at these regulatory regions, leading to the prevention of binding. Indeed, it has long been known that DNA methylation can prevent transcription factor binding leading to the inhibition of active transcription or the recruitment of methyl-binding proteins, causing gene suppression.[38] When looking for binding sites of important cell fate specificators in our tumor-specific methylated regions, we could indeed identify such a correlation, especially concerning the transcription factors NEUROD1, ZNF423, HAND1 and REST (Figure 2b).

ZNF423 (also known as Ebfaz, Roaz or Zfp423), a gene required for brain development,[41] may also have a role in neuroblastoma. ZNF423 is a transcription factor critically required for cerebellar development and retinoic acid-induced differentiation.[42] Downregulation of ZNF423 expression by RNA interference in neuroblastoma cells results in a growth advantage and resistance to retinoic acid-induced differentiation. Loss of the NF1 tumor suppressor activates RAS-MEK signaling, which in turn represses ZNF423, a critical transcriptional coactivator of the retinoic acid receptors. Neuroblastomas with low levels of both NF1 and ZNF423 have poor clinical outcome.[43]

REST/NRSF is a transcription factor involved in complex regulatory pathways controlling neuronal differentiation,[44] having both oncogenic and tumor-suppressive roles.[45] As shown in several other cancer types, there seems to be a correlation between the level of active REST and the tendency to initiate cancer.[46] Inactivation of the REST/NRSF network may have a role in derepression of some neuroendocrine genes in SCLC.[47] Interestingly, Kreisler *et al.*[48] found that three CpG islands associated with the *REST* gene were methylated in SCLC lines and we also found increased methylation near the *REST* promoter (Supplementary Figure 6). The loss of REST was linked to the malignant progression of SCLC.[48] We present evidence that methylation of *REST*-binding sites might also contribute to the SCLC phenotype.

Given that neuroendocrine cells are the likely cells of origin for SCLC,[10,11] it is interesting that a significant number of NEUROD1 potential binding sites were correlated with methylation in the tumors (Figure 2b). It has been shown in mice that NeuroD deficiency resulted in both impaired alveolar septation and altered morphology of the pulmonary neuroendocrine cells, suggesting a role in the regulation of pulmonary neuroendocrine and alveolar morphogenesis.[49] As such, methylation of NEUROD1-binding sites is supporting our theory of early methylation aberrations causing a defect in the developmental program of pulmonary neuroendocrine cells. Alternatively, lack of expression of transacting developmental transcription factors induced by methylation of their own promoter, which we did find for the *NEUROD1* gene (Supplementary Figure 6), could lead indirectly to methylation of the transcription factor target sites. In this scenario, methylation of the binding site regions of these factors is the default state and can be prevented by *in vivo* binding of the factor. Although hypothetical, our model has gained support from a recent study in mouse ES cells.[50] In this study, it was shown that the presence of several transcription factors, including REST, is required to create genomic regions with low DNA methylation.

In summary, we propose that probably both mechanisms, loss of key transcription factors involved in cell fate decisions or differentiation by methylation of their promoters, and functional inactivation of their corresponding binding site regions by methylation, can guide the cell of origin toward a malignant state. We note that this could be a potential explanation not only for the origin of SCLC but also for tumorigenesis in general.

MATERIALS AND METHODS

Tissue and DNA samples

Primary SCLC tumor tissue DNAs were obtained from patients undergoing surgery at the Nagoya University Hospital or Aichi Cancer Center, Nagoya, Japan. Pairs of human primary SCLC tumor tissue DNA and adjacent normal lung tissue DNA were obtained from Asterand (Detroit, MI, USA), BioChain (Hayward, CA, USA) and Cureline (South San Francisco, CA, USA). SCLC cell lines (H1688, H1417, H1836, DMS53 and SW1271) were obtained from the ATCC (Manassas, VA, USA). The ATCC used short tandem repeat profiling for cell line identification. Normal bronchial epithelial cells (HBECs obtained from Lonza, Walkersville, MD, USA) were used as a control for the cell line analysis. All cells were cultured with Dulbecco's modified Eagle's medium/F12 with 0.5% fetal bovine serum and the bronchial epithelial growth medium bullet kit (Lonza). DNA and RNA from the cell lines were extracted using the DNeasy Blood and Tissue Kit and RNeasy Mini Kit (Qiagen, Valencia, CA, USA), respectively.

MIRA and microarray hybridization

Tumor and normal tissue DNA was fragmented by sonication to ~500 bp average size as verified on agarose gels. Enrichment of the methylated double-stranded DNA fraction by MIRA was performed as described previously.[26,27] The labeling of amplicons, microarray hybridization and scanning were performed according to the NimbleGen (Madison, WI, USA) protocol. NimbleGen tiling arrays were used for hybridization (Human 3 × 720K CpG Island Plus RefSeq Promoter Arrays). These arrays cover all UCSC Genome Browser annotated CpG islands (total of 27 728) as well as the promoters (total of 22 532) of the well-characterized RefSeq genes derived from the UCSC RefFlat files. The promoter region covered is ~3 kb (−2440 to +610 relative to the transcription start sites). For all samples,

the MIRA-enriched DNA was compared with the input DNA. All microarray data sets have been deposited into the NCBI GEO database (accession number GSE35341).

Identification and annotation of methylated regions

Analysis of the arrays was performed with R version 2.10, Perl scripts and the Bioconductor package Ringo.[28] Arrays were clustered in normal tissues, cell lines and tumor tissues using hclust and Spearman's correlation. Biological replicates were quantile-normalized and arrays were normalized by Nimblegen's recommended method, tukey's biweight. Probe ratios were smoothed for three neighboring probes before peak calling. Instead of estimating a cutoff ratio based on a hypothetical normal distribution for non-bound probes (Ringo), a quantile-based approach was chosen to estimate methylation intensities. For this aim, peaks at different quantiles were called, where four probes were above the quantile-based threshold with a distance cutoff of 300 bp. A randomized set of peaks was validated by COBRA assays[51] for each quantile range. Thus, a quantile range of 80% was chosen as a cutoff for methylated regions (defined as hypermethylated regions). False positives and false negatives were assessed by COBRA. To investigate whether inter-sample differences had an influence on the acquired cutoff, predicted peaks were validated in different tissues by COBRA analysis.

Tumor-specific regions were defined using two different stringencies. In one case, an overlap of peaks in 6 or more out of 18 tumor samples (33%) was required above the cutoff quantile threshold of 80%; the genomic regions were defined and for those regions only one out of five normal tissues was allowed to overlap with a peak called on a 56% basis, which resulted in an at least 1.5 ratio change. Overlaps were calculated using BEDtools.[52] A more stringent analysis required an overlap of peaks in at least 14 out of 18 tumors (>77%), with the same settings as above. The obtained chromosomal positions were converted to the latest hg19 genome build, using LiftOver from UCSC, requiring a minimum ratio of 0.9 of bases that must remap. The obtained positions where then annotated using the Bioconductor package ChIPpeakAnno and the latest ensembl annotation from BioMart (Sanger Institute, Cambridge, UK).

Microarray expression analysis

Affymetrix (Santa Clara, CA, USA) human U133plus2.0 arrays for the three cell lines SW1271, H1836 and H1688 were processed by the robust multi-array average method implemented in the Bioconductor 'Affy' package, and the average log2 intensity of each gene across all samples was calculated. The three cell lines were clustered and compared against the control cell line, HBECs. Single expression values were obtained, using the MAS 5.0 method. Proximal promoter hypermethylated and non-hypermethylated regions, defined as −2000 to +1000 bp relative to transcription start sites according to the NimbleGen tilling arrays, were assigned with their respective expression probe changes of the corresponding transcript. The correlation between methylation and gene expression was based on a binary decision, linking gene promoters with differentially methylated regions with gene expression changes. A comparison with gene expression changes, where the promoter regions had a change in their methylation level (as measured by peak detected or absent), was above the significance threshold (*P*-value 0.05, two-sided *t*-test).

De novo motif prediction

Motif analysis was performed by HOMER, a program developed by Heinz *et al.*[35] More specifically, the discovery was performed using a comparative algorithm similar to those previously described by Linhart *et al.*[53] Briefly, sequences were divided into target and background sets for each application of the algorithm (choice of target and background sequences are noted below). Background sequences were then selectively weighted to equalize the distributions of CpG content in target and background sequences to avoid comparing sequences of different general sequence content. Motifs of length 8–30 bp were identified separately by first exhaustively screening all possible oligos for enrichment in the target set compared with the background set by assessing the number of target and background sequences containing each oligo and then using the cumulative hypergeometric distribution to score enrichment. Up to two mismatches were allowed in each oligonucleotide sequence to increase the sensitivity of the method. The top 200 oligonucleotides of each length with the best enrichment scores were then converted into basic probability matrices for further optimization. HOMER then generates motifs comprised of a position-weight matrix and detection threshold by empirically adjusting motif parameters to maximize the enrichment of motif instances in target sequences versus background sequences using the cumulative hypergeometric distribution as a scoring function. Probability matrix optimization follows a local hill-climbing approach that weights the contributions of individual oligos recognized by the motif to improve enrichment, while optimization of motif detection thresholds were performed by exhaustively screening degeneracy levels for maximal enrichment during each iteration of the algorithm. Once a motif is optimized, the individual oligos recognized by the motif are removed from the data set to facilitate the identification of additional motifs. Sequence logos were generated using WebLOGO (http://weblogo.berkeley.edu/). Motifs obtained from Jasper and TRANSFAC for which no high-throughput data exists were discarded for this analysis. Only those motifs with the highest alignments to known transcription factors, nonredundant matrixes and non-repetitive sequences were chosen for further analysis.

Functional annotation analysis

Gene ontology analysis was performed using DAVID functional annotation tools with Biological Process FAT and Molecular Function FAT data sets.[54,55] The enriched gene ontology terms were reported as clusters to reduce redundancy. The *P*-value for each cluster is the geometric mean of the *P*-values for all the GO categories in the cluster. The gene list in each cluster contains the unique genes pooled from the genes in all the GO categories in the cluster. Functional terms were clustered by using a Multiple Linkage Threshold of 0.5 and Bonferroni corrected *P*-values.

DNA methylation analysis using sodium bisulfite-based methods

DNA was treated and purified with the EZ DNA Methylation-Gold Kit (Zymo Research, Irvine, CA, USA). PCR primer sequences for amplification of specific gene targets in bisulfite-treated DNA are shown in Supplementary Table 17. The PCR products were analyzed by COBRA as described previously.[51] In addition, PCR products from bisulfite-converted DNA were cloned into pCR2.1-TOPO using a TOPO TA cloning kit (Invitrogen, Carlsbad, CA, USA), and individual clones were sequenced with M13 forward (−20) primer.

Transfection, reverse transcription and quantitative real-time PCR

The DMS53 SCLC line was transfected with a NEUROD1 expression plasmid (2 μg) at ~60% confluence in 35-mm dishes with FuGENE HD (Roche Applied Science, Indianapolis, IN, USA) in serum-free medium according to the manufacturer's recommendations. The cells were cultured for an additional 48 h for analysis of *NEUROD1* expression. Total RNA was isolated from HBECs, all five SCLC cell lines and from DMS53 cells overexpressing *NEUROD1* using the RNeasy Mini Kit (Qiagen). cDNA was prepared using the iScript cDNA synthesis kit (Bio-Rad; Hercules, CA, USA). Quantitative PCR was performed to assess expression of *NEUROD1* and 18S RNA using NEUROD1 primers (forward, 5′-GTTCTCAGGACGAGGAGCAC-3′and reverse 5′-CTTGGGCTTTTGATCGTCAT-3′) and 18S primers (forward 5′-GTAACCC GTTGAACCCCATT-3′ and reverse 5′-CCATCCAATCGGTAGTAGCG-3′). Real-time PCR was performed using iQ SYBR Green Supermix and the iCycler real-time PCR detection system (Bio-Rad). Amplicon expression in each sample was normalized to 18S RNA.

CONFLICT OF INTEREST

Under a licensing agreement between City of Hope and Active Motif (Carlsbad, CA, USA), the MIRA technique was licensed to Active Motif, and the author GPP is entitled to a share of the royalties received by City of Hope from sales of the licensed technology. The rest of the authors declare no conflict of interest.

ACKNOWLEDGEMENTS

We thank Steven Bates for culturing SCLC cell lines. This work was supported by the National Institutes of Health grant CA084469 to GPP and by generous funds from an anonymous donor.

REFERENCES

1 Govindan R, Page N, Morgensztern D, Read W, Tierney R, Vlahiotis A *et al.* Changing epidemiology of small-cell lung cancer in the United States over the last 30 years: analysis of the surveillance, epidemiologic, and end results database. *J Clin Oncol* 2006; **24**: 4539–4544.
2 Wistuba II, Gazdar AF, Minna JD. Molecular genetics of small cell lung carcinoma. *Semin Oncol* 2001; **28**: 3–13.

3 Sekido Y, Fong KM, Minna JD. Molecular genetics of lung cancer. *Annu Rev Med* 2003; **54**: 73–87.
4 Modi S, Kubo A, Oie H, Coxon AB, Rehmatulla A, Kaye FJ. Protein expression of the RB-related gene family and SV40 large T antigen in mesothelioma and lung cancer. *Oncogene* 2000; **19**: 4632–4639.
5 Johnson BE, Ihde DC, Makuch RW, Gazdar AF, Carney DN, Oie H *et al.* myc family oncogene amplification in tumor cell lines established from small cell lung cancer patients and its relationship to clinical status and course. *J Clin Invest* 1987; **79**: 1629–1634.
6 Little CD, Nau MM, Carney DN, Gazdar AF, Minna JD. Amplification and expression of the c-myc oncogene in human lung cancer cell lines. *Nature* 1983; **306**: 194–196.
7 Takahashi T, Obata Y, Sekido Y, Hida T, Ueda R, Watanabe H *et al.* Expression and amplification of myc gene family in small cell lung cancer and its relation to biological characteristics. *Cancer Res* 1989; **49**: 2683–2688.
8 Sattler M, Salgia R. Molecular and cellular biology of small cell lung cancer. *Semin Oncol* 2003; **30**: 57–71.
9 Fischer B, Marinov M, Arcaro A. Targeting receptor tyrosine kinase signalling in small cell lung cancer (SCLC): what have we learned so far? *Cancer Treat Rev* 2007; **33**: 391–406.
10 Sutherland KD, Proost N, Brouns I, Adriaensen D, Song JY, Berns A. Cell of origin of small cell lung cancer: inactivation of Trp53 and rb1 in distinct cell types of adult mouse lung. *Cancer Cell* 2011; **19**: 754–764.
11 Park KS, Liang MC, Raiser DM, Zamponi R, Roach RR, Curtis SJ *et al.* Characterization of the cell of origin for small cell lung cancer. *Cell Cycle* 2011; **10**: 2806–2815.
12 Sato M, Shames DS, Gazdar AF, Minna JD. A translational view of the molecular pathogenesis of lung cancer. *J Thorac Oncol* 2007; **2**: 327–343.
13 Dammann R, Li C, Yoon JH, Chin PL, Bates S, Pfeifer GP. Epigenetic inactivation of a RAS association domain family protein from the lung tumour suppressor locus 3p21.3. *Nat Genet* 2000; **25**: 315–319.
14 Lerman MI, Minna JD. The 630-kb lung cancer homozygous deletion region on human chromosome 3p21.3: identification and evaluation of the resident candidate tumor suppressor genes. The International Lung Cancer Chromosome 3p21.3 Tumor Suppressor Gene Consortium. *Cancer Res* 2000; **60**: 6116–6133.
15 Laird PW. The power and the promise of DNA methylation markers. *Nat Rev Cancer* 2003; **3**: 253–266.
16 Ushijima T. Detection and interpretation of altered methylation patterns in cancer cells. *Nat Rev Cancer* 2005; **5**: 223–231.
17 Burbee DG, Forgacs E, Zochbauer-Muller S, Shivakumar L, Fong K, Gao B *et al.* Epigenetic inactivation of RASSF1A in lung and breast cancers and malignant phenotype suppression. *J Natl Cancer Inst* 2001; **93**: 691–699.
18 Dammann R, Takahashi T, Pfeifer GP. The CpG island of the novel tumor suppressor gene RASSF1A is intensely methylated in primary small cell lung carcinomas. *Oncogene* 2001; **20**: 3563–3567.
19 Sunaga N, Miyajima K, Suzuki M, Sato M, White MA, Ramirez RD *et al.* Different roles for caveolin-1 in the development of non-small cell lung cancer versus small cell lung cancer. *Cancer Res* 2004; **64**: 4277–4285.
20 Kalari S, Pfeifer GP. Identification of driver and passenger DNA methylation in cancer by epigenomic analysis. *Adv Genet* 2010; **70**: 277–308.
21 Rauch TA, Pfeifer GP. DNA methylation profiling using the methylated-CpG island recovery assay (MIRA). *Methods* 2010; **52**: 213–217.
22 Rauch TA, Zhong X, Wu X, Wang M, Kernstine KH, Wang Z *et al.* High-resolution mapping of DNA hypermethylation and hypomethylation in lung cancer. *Proc Natl Acad Sci USA* 2008; **105**: 252–257.
23 Wu X, Rauch TA, Zhong X, Bennett WP, Latif F, Krex D *et al.* CpG island hypermethylation in human astrocytomas. *Cancer Res* 2010; **70**: 2718–2727.
24 Rauch T, Wang Z, Zhang X, Zhong X, Wu X, Lau SK *et al.* Homeobox gene methylation in lung cancer studied by genome-wide analysis with a microarray-based methylated CpG island recovery assay. *Proc Natl Acad Sci USA* 2007; **104**: 5527–5532.
25 Tommasi S, Karm DL, Wu X, Yen Y, Pfeifer GP. Methylation of homeobox genes is a frequent and early epigenetic event in breast cancer. *Breast Cancer Res* 2009; **11**: R14.
26 Rauch TA, Pfeifer GP. The MIRA method for DNA methylation analysis. *Methods Mol Biol* 2009; **507**: 65–75.
27 Rauch TA, Wu X, Zhong X, Riggs AD, Pfeifer GP. A human B cell methylome at 100-base pair resolution. *Proc Natl Acad Sci USA* 2009; **106**: 671–678.
28 Toedling J, Skylar O, Krueger T, Fischer JJ, Sperling S, Huber W. Ringo—an R/Bioconductor package for analyzing ChIP-chip readouts. *BMC Bioinformatics* 2007; **8**: 221.
29 Hahn MA, Hahn T, Lee DH, Esworthy RS, Kim BW, Riggs AD *et al.* Methylation of polycomb target genes in intestinal cancer is mediated by inflammation. *Cancer Res* 2008; **68**: 10280–10289.
30 Reinert T, Modin C, Castano FM, Lamy P, Wojdacz TK, Hansen LL *et al.* Comprehensive genome methylation analysis in bladder cancer: identification and validation of novel methylated genes and application of these as urinary tumor markers. *Clin Cancer Res* 2011; **17**: 5582–5592.
31 Rodriguez J, Munoz M, Vives L, Frangou CG, Groudine M, Peinado MA. Bivalent domains enforce transcriptional memory of DNA methylated genes in cancer cells. *Proc Natl Acad Sci USA* 2008; **105**: 19809–19814.
32 Takeshima H, Yamashita S, Shimazu T, Niwa T, Ushijima T. The presence of RNA polymerase II, active or stalled, predicts epigenetic fate of promoter CpG islands. *Genome Res* 2009; **19**: 1974–1982.
33 Kondo Y, Shen L, Cheng AS, Ahmed S, Boumber Y, Charo C *et al.* Gene silencing in cancer by histone H3 lysine 27 trimethylation independent of promoter DNA methylation. *Nat Genet* 2008; **40**: 741–750.
34 Maunakea AK, Nagarajan RP, Bilenky M, Ballinger TJ, D'Souza C, Fouse SD *et al.* Conserved role of intragenic DNA methylation in regulating alternative promoters. *Nature* 2010; **466**: 253–257.
35 Heinz S, Benner C, Spann N, Bertolino E, Lin YC, Laslo P *et al.* Simple combinations of lineage-determining transcription factors prime cis-regulatory elements required for macrophage and B cell identities. *Mol Cell* 2010; **38**: 576–589.
36 Lee NH, Haas BJ, Letwin NE, Frank BC, Luu TV, Sun Q *et al.* Cross-talk of expression quantitative trait loci within 2 interacting blood pressure quantitative trait loci. *Hypertension* 2007; **50**: 1126–1133.
37 Piper M, Barry G, Hawkins J, Mason S, Lindwall C, Little E *et al.* NFIA controls telencephalic progenitor cell differentiation through repression of the Notch effector Hes1. *J Neurosci* 2010; **30**: 9127–9139.
38 Suzuki MM, Bird A. DNA methylation landscapes: provocative insights from epigenomics. *Nat Rev Genet* 2008; **9**: 465–476.
39 Hanahan D, Weinberg RA. Hallmarks of cancer: the next generation. *Cell* 2011; **144**: 646–674.
40 Smith LT, Lin M, Brena RM, Lang JC, Schuller DE, Otterson GA *et al.* Epigenetic regulation of the tumor suppressor gene TCF21 on 6q23-q24 in lung and head and neck cancer. *Proc Natl Acad Sci USA* 2006; **103**: 982–987.
41 Warming S, Rachel RA, Jenkins NA, Copeland NG. Zfp423 is required for normal cerebellar development. *Mol Cell Biol* 2006; **26**: 6913–6922.
42 Huang S, Laoukili J, Epping MT, Koster J, Holzel M, Westerman BA *et al.* ZNF423 is critically required for retinoic acid-induced differentiation and is a marker of neuroblastoma outcome. *Cancer Cell* 2009; **15**: 328–340.
43 Holzel M, Huang S, Koster J, Ora I, Lakeman A, Caron H *et al.* NF1 is a tumor suppressor in neuroblastoma that determines retinoic acid response and disease outcome. *Cell* 2010; **142**: 218–229.
44 Qureshi IA, Gokhan S, Mehler MF. RESTand CoREST are transcriptional and epigenetic regulators of seminal neural fate decisions. *Cell Cycle* 2010; **9**: 4477–4486.
45 Majumder S. REST in good times and bad: roles in tumor suppressor and oncogenic activities. *Cell Cycle* 2006; **5**: 1929–1935.
46 Coulson JM. Transcriptional regulation: cancer, neurons and the REST. *Curr Biol* 2005; **15**: R665–R668.
47 Coulson JM, Edgson JL, Woll PJ, Quinn JP. A splice variant of the neuron-restrictive silencer factor repressor is expressed in small cell lung cancer: a potential role in derepression of neuroendocrine genes and a useful clinical marker. *Cancer Res* 2000; **60**: 1840–1844.
48 Kreisler A, Strissel PL, Strick R, Neumann SB, Schumacher U, Becker CM. Regulation of the NRSF/REST gene by methylation and CREB affects the cellular phenotype of small-cell lung cancer. *Oncogene* 2010; **29**: 5828–5838.
49 Neptune ER, Podowski M, Calvi C, Cho JH, Garcia JG, Tuder R *et al.* Targeted disruption of NeuroD, a proneural basic helix-loop-helix factor, impairs distal lung formation and neuroendocrine morphology in the neonatal lung. *J Biol Chem* 2008; **283**: 21160–21169.
50 Stadler MB, Murr R, Burger L, Ivanek R, Lienert F, Scholer A *et al.* DNA-binding factors shape the mouse methylome at distal regulatory regions. *Nature* 2011; **480**: 490–495.
51 Xiong Z, Laird PW. COBRA: a sensitive and quantitative DNA methylation assay. *Nucleic Acids Res* 1997; **25**: 2532–2534.
52 Quinlan AR, Hall IM. BEDTools: a flexible suite of utilities for comparing genomic features. *Bioinformatics* 2010; **26**: 841–842.
53 Linhart C, Halperin Y, Shamir R. Transcription factor and microRNA motif discovery: the Amadeus platform and a compendium of metazoan target sets. *Genome Res* 2008; **18**: 1180–1189.
54 Huang da W, Sherman BT, Lempicki RA. Systematic and integrative analysis of large gene lists using DAVID bioinformatics resources. *Nat Protoc* 2009; **4**: 44–57.
55 Huang da W, Sherman BT, Lempicki RA. Bioinformatics enrichment tools: paths toward the comprehensive functional analysis of large gene lists. *Nucleic Acids Res* 2009; **37**: 1–13.

Supplementary Information accompanies the paper on the Oncogene website (http://www.nature.com/onc)

Bioorganic & Medicinal Chemistry Letters 22 (2012) 1731–1733

Contents lists available at SciVerse ScienceDirect

Bioorganic & Medicinal Chemistry Letters

journal homepage: www.elsevier.com/locate/bmcl

Hybrid liposomes affect cellular lipid constituents and caveolae structures

Ke Cao [a], Kouji Tanaka [b], Yuji Komizu [c], Keiko Tamiya-Koizumi [d], Takashi Murate [d], Ryuichi Ueoka [c], Mamoru Kyogashima [e], Jiro Usukura [f], Takashi Takahashi [a], Motoshi Suzuki [a,*]

[a] Division of Molecular Carcinogenesis, Nagoya University Graduate School of Medicine, Nagoya 466-8550, Japan
[b] Department of Oncology, Graduate School of Pharmaceutical Science, Nagoya City University, Nagoya 464-8681, Japan
[c] Division of Applied Life Science, Graduate School of Engineering, Sojo University, Kumamoto 860-0082, Japan
[d] Department of Medical Technology, Nagoya University Graduate School of Health Sciences, Nagoya 461-8673, Japan
[e] Department of Microbiology and Molecular Cell Biology, Nihon Pharmaceutical University, Saitama 362-0806, Japan
[f] Research Facility in Advanced Science and Technology, EcoTopia Science Institute, Nagoya University, Nagoya 464-8603, Japan

ARTICLE INFO

Article history:
Received 25 October 2011
Revised 5 December 2011
Accepted 20 December 2011
Available online 28 December 2011

Keywords:
Hybrid liposomes
Phosphatidylcholine
Cancer
Caveolae

ABSTRACT

We examined alterations of lipid constituents induced by hybrid liposomes (HLs) in cancer cells. As early as 1 h after HL treatment, amounts of the raft/caveolae lipids sphingomyelin, ceramide, and ether-type PC were altered. In addition, the structures of caveolae on the cytoplasmic surface of the cell membrane were significantly changed. Our results suggest that alterations of lipid composition in caveolae mediate HL signaling for apoptosis.

Hybrid liposomes† (HLs)[1] contain 90 mol % L-α-dimyristoylphosphatidylcholine (DMPC, NOF, Tokyo, Japan) and 10 mol % polyoxyethylene(n) dodecyl ether ($C_{12}(EO)_n$, $n = 23$, Sigma Chemicals, St Louis, MO) in a 5% glucose solution.[2] They have been shown effective for inhibiting the growth of various tumor cells in vitro,[3,4] in vivo in animal models,[5,6] and in a clinical patient.[7]

HLs are fused and accumulate in tumor cell membranes, and their apoptosis signals are passed through caspases-9, -3, and -8.[2] However, which signals initially activate these apoptotic pathways have yet to be elucidated. In that regard, we analyzed the lipid constituents in HL-treated SH-SY5Y and LS174T cells.

In accord with previous results, HLs reduced the viable cell population (Fig. 1). Under these conditions, the total amounts of the glycerophospholipids PC, PE, PI, and PS were not significantly different between the HL-treated and control cells (Supplementary Fig. 1).

Since DMPC is the major HL component, we further analyzed PC species. In the absence of HLs, we were unable to detect DMPC in SH-SY5Y and LS174T cells. In contrast, HL-treated cells were found to contain DMPC, and had decreased amounts of ether- and other types of diacyl-PC (Fig. 2A, B). Also, MALDI-TOF MS analysis revealed that in addition to DMPC, the levels of PC with C30:0 (hereinafter abbreviated as C30:0) in SH-SY5Y cells and C32:1 in LS174T were also increased (Fig. 2C, D). C30:0 and C32:1 may be metabolic products of DMPC, generated by re-acylation of excised and elongated myristic acid. In contrast, the cells were associated with a global decrease in PC species with longer acyl chains.

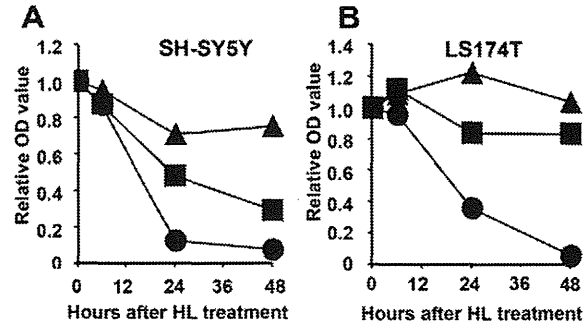

Figure 1. Apoptosis induction. SH-SY5Y (A) or LS-174T (B) cells were cultured in 500 μl of culture medium in 24-well plates at a density of 5×10^4 per well for 16 h. Medium was replaced with that containing various concentrations of HLs, followed by incubation for up to 48 h. Viable cells were determined in triplicate using TetraColor One (Seikagaku, Tokyo, Japan) with reference to the viability of mock-treated cells.[8] Triangle, square, and circle represent cells treated with 50, 100 and 200 μM, respectively, of HLs. Error bars are shown when errors exceed the symbols.

* Corresponding author. Tel.: +81 52 744 2456; fax: +81 52 744 2457.
E-mail address: msuzuki@med.nagoya-u.ac.jp (M. Suzuki).

† Abbreviations: HLs, hybrid liposomes; PC, phosphatidylcholine; DMPC, dimyristoylphosphatidylcholine; PC, PE, PI and PS are glycerophospholipid containing choline, ethanolamine, inositol and serine.

0960-894X/$ - see front matter © 2011 Elsevier Ltd. All rights reserved.
doi:10.1016/j.bmcl.2011.12.093

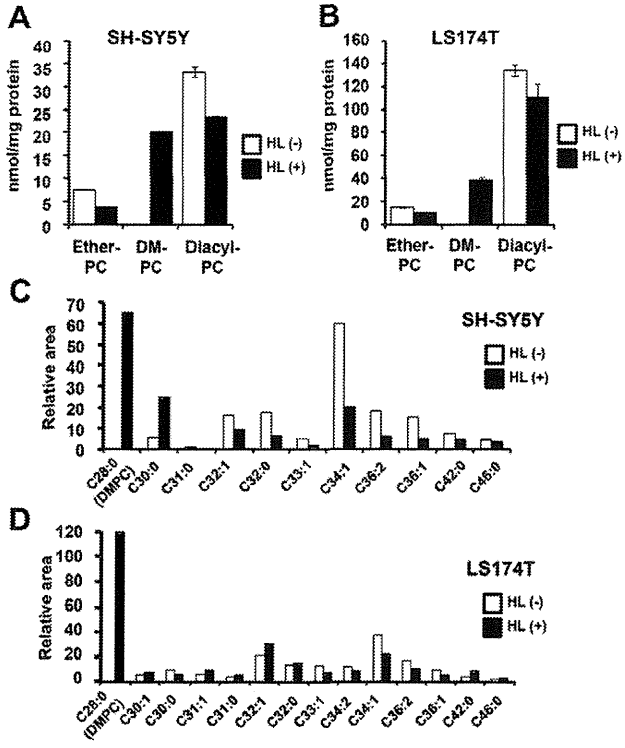

Figure 2. Molecular species of PC. (A, B) Total PC prepared by Folch's method[9] was subjected to mild alkaline hydrolysis.[10] An alkali-stable PC fraction containing an alkenyl- or alkyl-chain was designated as ether-PC. The amount of diacyl-PC was calculated by subtracting the amounts of ether- and DM-PC from total PC. (C, D). PC species were analyzed in positive ion mode using an AXIMA Performance mass spectrometer (Shimadzu/Kratos, UK) equipped with a nitrogen UV laser (337 nm). Sphingosylphosphorylcholine was mixed with the PC extracts, and used as the standard. Areas corresponding to each PC were calculated and are shown as graphs. DMPC was designated as C28:0. HL (+) and HL (−) represent results obtained with and without HLs, respectively.

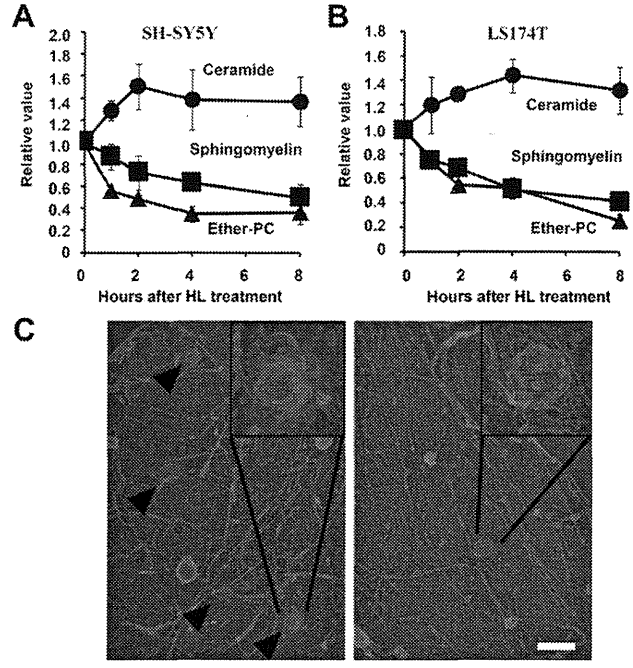

Figure 3. Alterations in caveolae constituents and structures. (A, B) Ceramide was separated from total lipids by thin-layer chromatography (TLC) and developed using $CHCl_3$/MeOH/acetic acid (94:1:5, v/v). Sphingomyelin and ether-PC (Fig. 2) were separated from alkali-stable lipid fractions by TLC, and developed using $CHCl_3$/MeOH/H_2O (65:25:4, v/v). Each lipid band was visualized after spraying 0.1% primulin in acetone/H_2O (Sigma, >4:1,v/v) and UV irradiation, and quantified using ImageJ (NIH, Bethesda, MD). Intensity at 0 h was designated as 1. (C) SH-SY5Y cells were cultured with 200 μM HL for 0 (left) or 1 (right) hour, then their submembrane structures were subjected to ultramicroscopic analysis. Arrowheads indicate caveolae. Some are enlarged and shown in inlets. White bar indicates 1 μm.

Among the sphingolipids, HL treatment resulted in a decrease in sphingomyelin and an increase in ceramide (Fig. 3A, B), as early as 1 h after HL addition. HL addition might have induced hydrolysis of sphingomyelin by neutral sphingomyelinases in the plasma membrane, resulting in ceramide production. It is also likely that DMPC competitively inhibited sphingomyelin synthases, which catalyse phosphocholine transfer from PC to ceramide. This inhibition may lead to ceramide increase and sphingomyelin decrease. It was also found that ether-PC was decreased in a similar manner as sphingomyelin (Fig. 3A, B).

Since sphingolipids and ether-PC are the major components of the detergent-resistant membrane micro-domain raft/caveolae,[11–13] alterations of these lipids may affect the structures and functions of members of this micro-domain. To investigate these phenomena, we visualized the membrane undercoat of the vertical cell surface using a freeze-etching replica method.[14] One hour after HL treatment, we found a change in the membrane skeleton. In control cells, actin filaments extended over the membrane surface, whereas they were firmly attached to the surface in the HL-treated cells. Furthermore, we were unable to find typical caveolae structures in HL-treated cells, except for distorted structures (Fig. 3C).

In summary, HL treatment altered the amounts of ether-PC, sphingomyelin, and ceramide, which may have also resulted in alterations of the caveolae structures. Since caveolae play essential roles in signal transduction, the HL-treated cells likely generated ill-signals and fallen into apoptosis. It has been proposed that ceramide plays an important role in the apoptotic signaling pathway.[15,16] Therefore, we do not rule out the possibility that a certain type of ceramide played a role as a second messenger, leading to apoptosis. In this manuscript, we have focused on the alterations in the phospho- and sphingolipids compositions. With the concentration employed in our experiments, contribution extent of $C_{12}(EO)_{23}$, the second component of HL, to apoptosis signaling may be limited, because $C_{12}(EO)_{23}$ has been primarily considered to function for vesicle -fluidity and -uptake into cells.[17–20] Further analysis and identification of HL-induced apoptosis pathways may provide the basis for future cancer treatment.

Acknowledgments

This work was supported in part by a Grant-in-Aid for Scientific Research on Innovative Areas from the Ministry of Education, Culture, Sports, Science, and Technology of Japan, and a Grant-in-Aid for Scientific Research from the Japan Society for the Promotion of Science. We thank Dr. Mitsuhiro Nakamura of Gifu Pharmaceutical University and Dr. Yoshiko Banno for Gifu University Graduate School of Medicine for the critical discussion.

Supplementary data

Supplementary data associated with this article can be found, in the online version, at doi:10.1016/j.bmcl.2011.12.093.

References and notes

1. Ueoka, R.; Matsumoto, Y.; Robert, A.; Swarup, S.; Sugii, A.; Harada, K.; Kikuchi, J.; Murakami, Y. *J. Am. Chem. Soc.* **1988**, *110*, 1588.
2. Matsumoto, Y.; Iwamoto, Y.; Matsushita, T.; Ueoka, R. *Int. J. Cancer* **2005**, *115*, 377.
3. Komizu, Y.; Nakata, S.; Goto, K.; Matsumoto, Y.; Ueoka, R. A. C. S. *Med. Chem. Lett.* **2011**, *2*, 275.

4. Towata, T.; Komizu, Y.; Kariya, R.; Suzu, S.; Matsumoto, Y.; Kobayashi, N.; Wongkham, C.; Wongkham, S.; Ueoka, R.; Okada, S. *Bioorg. Med. Chem. Lett.* **2010**, *20*, 3680.
5. Ichihara, H.; Ueno, J.; Umebayashi, M.; Matsumoto, Y.; Ueoka, R. *Int. J. Pharm.* **2011**, *406*, 173.
6. Towata, T.; Komizu, Y.; Suzu, S.; Matsumoto, Y.; Ueoka, R.; Okada, S. *Leuk. Res.* **2010**, *34*, 906.
7. Ichihara, H.; Nagami, H.; Kiyokawa, T.; Matsumoto, Y.; Ueoka, R. *Anticancer Res.* **2008**, *28*, 1187.
8. Huang, Q. M.; Tomida, S.; Masuda, Y.; Arima, C.; Cao, K.; Kasahara, T. A.; Osada, H.; Yatabe, Y.; Akashi, T.; Kamiya, K.; Takahashi, T.; Suzuki, M. *Cancer Res.* **2010**, *70*, 8407.
9. Folch, J.; Lees, M.; Sloane Stanley, G. H. *J. Biol. Chem.* **1957**, *226*, 497.
10. Dawson, R. M. *Biochem. J.* **1960**, *75*, 45.
11. Kiyokawa, E.; Baba, T.; Otsuka, N.; Makino, A.; Ohno, S.; Kobayashi, T. *J. Biol. Chem.* **2005**, *280*, 24072.
12. Matsumori, N.; Okazaki, H.; Nomura, K.; Murata, M. *Chem. Phys. Lipids* **2011**, *164*, 401.
13. Milhas, D.; Clarke, C. J.; Hannun, Y. A. *FEBS Lett.* **2010**, *584*, 1887.
14. Morone, N.; Fujiwara, T.; Murase, K.; Kasai, R. S.; Ike, H.; Yuasa, S.; Usukura, J.; Kusumi, A. *J. Cell Biol.* **2006**, *174*, 851.
15. Hannun, Y. A. *Science* **1996**, *274*, 1855.
16. Stiban, J.; Tidhar, R.; Futerman, A. H. *Adv. Exp. Med. Biol.* **2010**, *688*, 60.
17. Kao, K. N.; Constabel, F.; Michayluk, M. R.; Gamborg, O. L. *PLANTA* **1974**, *115*, 355.
18. Nagami, H.; Matsumoto, Y.; Ueoka, R. *Int. J. Pharm.* **2006**, *315*, 167.
19. Komizu, Y.; Ueoka, H.; Goto, K.; Ueoka, R. *Int. J. Nanomedicine* **2011**, *6*, 1913.
20. Komizu, Y.; Yukihara, M.; Kariya, R.; Goto, K.; Okada, S.; Ueoka, R. *Bioorg. Med. Chem. Lett.* **2011**, *21*, 3962.

Cancer Research

Tumor Cell–Derived Angiopoietin-like Protein ANGPTL2 Is a Critical Driver of Metastasis

Motoyoshi Endo[1], Masahiro Nakano[1,2], Tsuyoshi Kadomatsu[1], Shigetomo Fukuhara[3], Hiroaki Kuroda[4], Shuji Mikami[5], Tai Hato[4,6], Jun Aoi[1], Haruki Horiguchi[1], Keishi Miyata[1], Haruki Odagiri[1], Tetsuro Masuda[1], Masahiko Harada[6], Hirotoshi Horio[6], Tsunekazu Hishima[7], Hiroaki Nomori[4], Takaaki Ito[8], Yutaka Yamamoto[2], Takashi Minami[9], Seiji Okada[10], Takashi Takahashi[11], Naoki Mochizuki[3], Hirotaka Iwase[2], and Yuichi Oike[1]

Abstract

Strategies to inhibit metastasis have been mainly unsuccessful in part due to insufficient mechanistic understanding. Here, we report evidence of critical role for the angiopoietin-like protein 2 (ANGPTL2) in metastatic progression. In mice, *Angptl2* has been implicated in inflammatory carcinogenesis but it has not been studied in human tumors. In patients with lung cancer, elevated levels of ANGPTL2 expression in tumor cells within the primary tumor were associated with a reduction in the period of disease-free survival after surgical resection. Transcription factors NFATc, ATF2, and c-Jun upregulated in aggressive tumor cells promoted increased *Angptl2* expression. Most notably, tumor cell–derived ANGPTL2 increased *in vitro* motility and invasion in an autocrine/paracrine manner, conferring an aggressive metastatic tumor phenotype. In xenograft mouse models, tumor cell–derived ANGPTL2 accelerated metastasis and shortened survival whereas attenuating ANGPTL2 expression in tumor cells–blunted metastasis and extended survival. Overall, our findings showed that tumor cell–derived ANGPTL2 drives metastasis and provided an initial proof of concept for blockade of its action as a strategy to antagonize the metastatic process. *Cancer Res; 72(7); 1784–94. ©2012 AACR.*

Introduction

Cancer is a leading cause of death and accounts for 7.6 million deaths (~13% of all deaths) worldwide (1). Although both diagnosis and therapeutic modalities used to treat cancer have remarkably improved, tumor metastasis still represents a major cause of cancer mortality (2, 3). Therefore, identification of mechanisms underlying metastasis is essential to understand the pathophysiology of this lethal condition and identify novel therapeutic targets.

Authors' Affiliations: Departments of [1]Molecular Genetics, [2]Breast and Endocrine Surgery, Kumamoto University, Kumamoto; [3]Department of Structural Analysis, National Cardiovascular Center Research Institute, Osaka; Departments of [4]General Thoracic Surgery and [5]Diagnostic Pathology, Keio University; Departments of [6]General Thoracic Surgery and [7]Pathology, Tokyo Metropolitan Cancer and Infectious Diseases Center Komagome Hospital; [8]Departments of Pathology and Experimental Medicine, Kumamoto University, Kumamoto; [9]Research Center for Advanced Science and Technology, University of Tokyo, Tokyo; and [10]Center for AIDS Research Center, Kumamoto University, Kumamoto; and [11]Division of Molecular Carcinogenesis, Center for Neurological Diseases and Cancer, Nagoya University Graduate School of Medicine, Nagoya, Japan

Note: Supplementary data for this article are available at Cancer Research Online (http://cancerres.aacrjournals.org/).

M. Endo, M. Nakano, and T. Kadomatsu contributed equally to this work.

Corresponding Author: Yuichi Oike, Department of Molecular Genetics, Kumamoto University, 1-1-1 Honjo, Kumamoto 860-8556, Japan. Phone: 81-96-373-5140; Fax: 81-96-373-5145; E-mail: oike@gpo.kumamoto-u.ac.jp

doi: 10.1158/0008-5472.CAN-11-3878

Inflammation plays key roles at various stages of tumor development, including initiation, growth, invasion, and metastasis (4). Recently, we found that angiopoietin-like protein 2 (ANGPTL2) increases inflammatory carcinogenesis in a chemically induced skin squamous cell carcinoma (SCC) mouse model through enhanced susceptibility to "preneoplastic change" and "malignant conversion" (5). In addition, we also reported that ANGPTL2 expression in tumor cells is highly correlated with the frequency of tumor cell metastasis to distant organs and lymph nodes through increased tumor angiogenesis and tumor cell epithelial-to-mesenchymal transitions (EMT; ref. 5). However, it has been obscure whether ANGPTL2 contributes to human cancer pathogenesis.

The nuclear factor of activated T cell (NFATc) consists of 5 members (NFATc1–c4 and NFAT5). Among these factors, NFATc1–c4 function in tumor cell development and metastasis (6, 7). For example, NFATc1 and NFATc3 contribute to the pathogenesis of melanoma and pancreatic cancer (8, 9), NFATc2 plays role in breast cancer cell migration and invasion (10), and NFATc4 promotes breast cancer cell growth (11).

In the present study, we investigated the role of ANGPTL2 in human tumor cells and found that patients with lung cancer showing high ANGPTL2 expression in cells within the primary tumor sites showed poor prognosis in terms of disease-free survival. Furthermore, we found that *Angptl2* expression in tumor cells is induced by NFATc. Tumor cell–derived ANGPTL2 enhanced tumor cell motility and invasive capacity and increased tumor angiogenesis. Tumor cell–derived ANGPTL2 also accelerated metastasis and shortened survival periods in tumor cell–implanted mouse models. In contrast,

decreasing ANGPTL2 levels in tumor cells attenuated metastasis and prolonged survival periods. Collectively, our findings provide strong evidence that tumor cell–derived ANGPTL2 worsens clinical prognosis and suggest that blocking ANGPTL2 could represent a novel therapeutic strategy to inhibit tumor metastasis.

Materials and Methods

Quantitation of ANGPTL2 protein by ELISA

ANGPTL2 concentrations in tissue lysates or in culture medium from tumor cells were estimated by an ANGPTL2 Assay Kit (IBL), as described (12, 13). For tissue lysates, proteins were extracted from 2 mg of tumor or nontumor tissue and dissolved in 10 mL lysis buffer [300 mmol/L NaCl, 50 mmol/L Tris-HCl (pH 7.5), 1% Triton X-100, and 1mmol/L EDTA].

Immunohistochemistry and *in situ* hybridization

Immunohistochemical and *in situ* hybridization analyses were conducted as described (12, 14). Antibodies for CD44 (Abcam), paxillin (BD Bioscience), and rhodamine-phalloidin (Molecular Probes) were purchased. We also used an anti-ANGPTL2 antibody that we generated (12, 14).

Cell lines and cell culture

The human lung cancer cell lines NCI-H460 and NCI-H460-LNM35 cells, as previously described (15), were provided by T. Takahashi (Nagoya University, Nagoya, Japan). H460 and LNM35 cells were cultured in RPMI-1640 medium supplemented with 10% fetal calf serum. The human breast adenocarcinoma cell lines T47D, MDA-MB453, and MDA-MB231 were purchased from the American Type Culture Collection that carries out cell line characterizations and passaged in our laboratory for fewer than 6 months after receipt. Detailed information about establishment of stable cell lines is provided in the Supplementary Methods.

Luciferase assay

H460 cells were incubated for 48 hours after cotransfection with indicated expression and reporter plasmids and phRL-TK vector (Promega). Luciferase activities were determined by a Dual-Luciferase Reporter Assay System (Promega). For some experiments, transfected cells were incubated with 10 ng/mL phorbol 12-myristate 13-acetate (PMA) or with 10 ng/mL PMA plus 1 μmol/L ionomycin (PMA/Ion) for 24 hours. Details relevant to expression and reporter plasmids are provided in the Supplementary Methods.

Real-time quantitative reverse transcriptase PCR

Real-time quantitative reverse transcriptase PCR was carried out as described (12). Oligonucleotide primers are listed in Supplementary Table S1.

Immunoblot analysis

Immunoblot analysis was conducted as described (5). Antibodies used were against NFATc2 (BD Bioscience), ATF2 (N-96; Santa Cruz), c-Jun (D; Santa Cruz), and ANGPTL2 (13).

Cell invasion assay

Cell invasiveness was estimated by a 96-well BME Cell Invasion Assay Kit (Trevigen) according to the manufacturer's protocol. Fluorescence was measured with a Fluoroskan Ascent fluorometer (Thermo Labsystems).

Time-lapse microscopy and FRET imaging

Cell migration was monitored by time-lapse microscopy with an Olympus IX-81 inverted microscope with a 20× objective lens. Phase contrast images were collected with CoolSNAP-HQ (Roper Scientific) at 3-minute intervals. A series of time-lapse images was converted to video format with MetaMorph 6.1 software. Cell motility was quantified with MetaMorph 6.1 software. Fluorescence resonance energy transfer (FRET) imaging was carried out as described (13).

Human studies

All studies were approved by the Ethics Committee of Kumamoto University, Keio University (Tokyo, Japan), or the Tokyo Metropolitan Cancer and Infectious Diseases Center of Komagome Hospital. Written informed consent was obtained from each subject. Patient information is provided in Supplementary Methods.

Animal studies

All experiments were carried out according to guidelines of Institutional Animal Committee of Kumamoto University. Details relevant to the mouse model are provided in Supplementary Methods.

Statistics

The Kaplan–Meier log-rank test was used to analyze survival data of mice and patients with JMP7 software (SAS Institute). Data presented as means ± SD or means ± SEM were analyzed using the Student *t* test or ANOVA. A P value of less than 0.05 was considered significant.

Results

ANGPTL2 levels within primary tumor sites correlate with poor disease-free survival

To examine whether ANGPTL2 is expressed in human tumor tissues, we compared ANGPTL2 protein levels in lung tissues extracted from primary tumor sites in patients with non–small cell lung carcinoma (NSCLC) to those from peripheral nontumor lung tissue by an ELISA. ANGPTL2 protein levels in primary tumor sites were significantly greater than those seen in nontumor lung tissue (Fig. 1A). Given the variation in ANGPTL2 expression in tumor tissue (Fig. 1A), we examined ANGPTL2 expression in lung tumor tissues by immunohistochemistry. Accordingly, we observed wide variation in the proportion of cells within a tumor that express ANGPTL2 (Fig. 1B, Supplementary Fig. S1). *In situ* hybridization analysis (12) confirmed that tumor cells express *Angptl2* mRNA (Fig. 1C), indicating that tumor cells are the likely source of ANGPTL2 protein. In contrast to the variation in the proportion of ANGPTL2-expressing tumor cells within the primary tumor site, we observed high and homogeneous

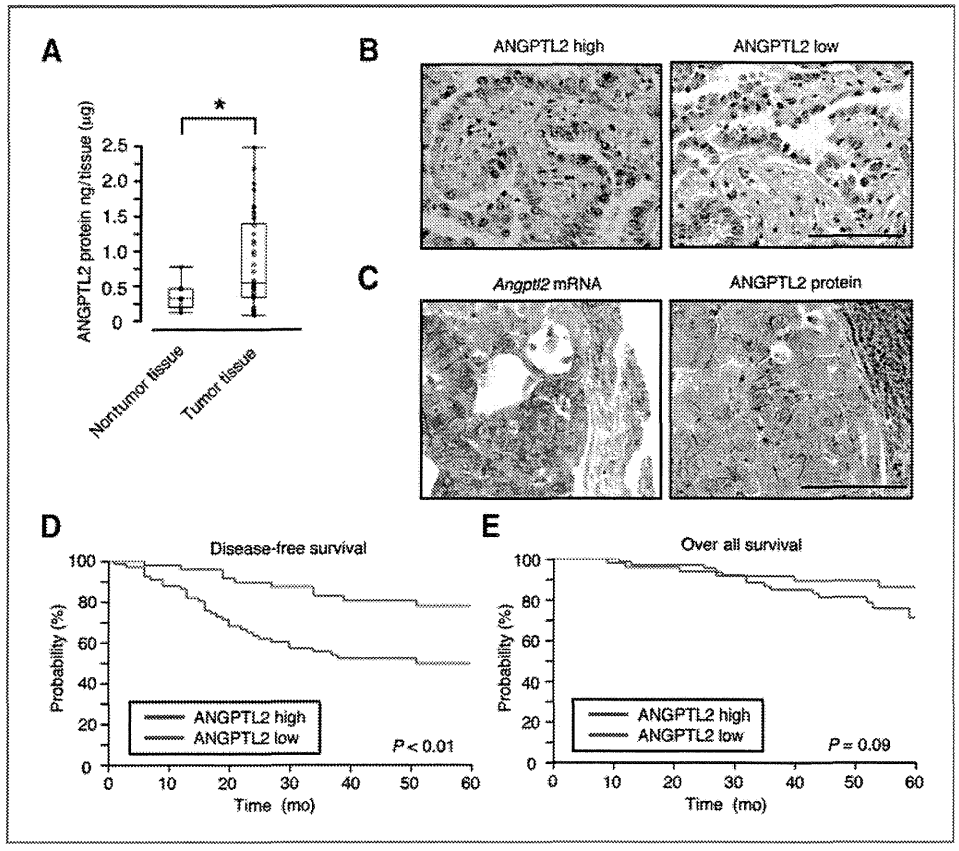

Figure 1. ANGPTL2 expression in tumor cells correlates with poor lung cancer prognosis. A, ANGPTL2 protein levels in lung tumor tissues ($n = 38$) and corresponding peripheral nontumor tissues ($n = 9$). B, ANGPTL2 immunostaining within the primary tumor. Groups from patients with NSCLC were defined as ANGPTL2 high and low, respectively. Scale bars, 100 μm. C, representative images of *Angptl2* mRNA and protein in serial tumor tissue sections from primary NSCLC. Scale bars, 100 μm. D–E, cohort of probability of disease-free survival (D) and overall survival (E) with ANGPTL2 high ($n = 66$) and low ($n = 48$) groups ($P < 0.01$ and $P = 0.09$ by log-rank test). *, $P < 0.05$.

expression of ANGPTL2 in tumor cells within metastasized tumor sites, including 3 brain tissues and 5 lymph nodes taken from 8 patients with lung cancer at autopsy (Supplementary Fig. S2), suggesting that ANGPTL2-positive tumor cells exhibit high metastatic capacity. We next divided patients with NSCLC into 2 groups based on the percentage of ANGPTL2-positive tumor cells within the primary tumor site: the high group was defined as showing greater than 20% of ANGPTL2-positive tumor cells and the low group showed fewer than 20%. Patients in the high group showed a shortened period of disease-free survival after surgery compared with the low group based on 2 independent cohort studies (Fig. 1D and E, Supplementary Fig. S3).

NFATc induces *Angptl2* expression in lung cancer cells

To investigate tumor cell regulation of *Angptl2* expression, we constructed luciferase reporter plasmids containing an *Angptl2* regulatory region that we identified from the human NSCLC cell line NCI-H460 (H460; Supplementary Fig. S4A). An F4 construct containing nucleotides −168 to +98 relative to the transcription start site of human *Angptl2* showed high reporter activity in H460 cells, whereas activity of an F5 construct (containing −21 to +98) showed significantly decreased activity, indicating that F4 contains elements regulate *Angptl2* expression in this context (Supplementary Fig. S4A). In that region, we identified potential binding sites for activating transcription factor/cAMP-responsive element–binding protein (ATF/CREB), NF-κB, and NFAT (Fig. 2A, top). To investigate whether these factors affect *Angptl2* expression, we transfected H460 cells with the F4 construct plus expression vectors encoding CREB, ATF2, ATF3, NF-κB, or a constitutively active form of NFATc (CA-NFATc). The CA-NFATc vector increased *Angptl2* reporter activity relative to a pcDNA3.1 control plasmid, whereas the other factors had no effect (Fig. 2A). Treatment of cells with a combination of PMA and ionomycin (PMA/Ion) stimulates calcium/calcineurin-dependent NFATc activation and induces its nuclear translocation (6, 16, 17). PMA/Ion treatment of H460 cells significantly increased *Angptl2* mRNA expression compared with controls, whereas treatment with the calcineurin inhibitor cyclosporin A (CsA) significantly blocked the PMA/Ion effect (Fig. 2B). These results suggest that NFATc functions in *Angptl2* expression in lung cancer cells.

ATF2 and c-Jun enhance NFATc-dependent *Angptl2* expression in lung cancer cells

It has been reported that activator protein (AP-1) components, c-Jun or c-Fos, form a stable heterodimer with ATF2, ATF3, or ATF4 and bind to the ATF/CREB site (18, 19). NFATc and AP-1 heterodimers form a transcriptional complex that synergistically activates target genes (20–22). We found that reporter activity of F4 constructs containing a mutant ATF/CREB site was markedly decreased relative to wild-type F4 constructs (Supplementary Fig. S4B), suggesting that ATF/CREB site is required for *Angptl2* expression. We observed that CA-NFATc–dependent induction of *Angptl2* reporter activity

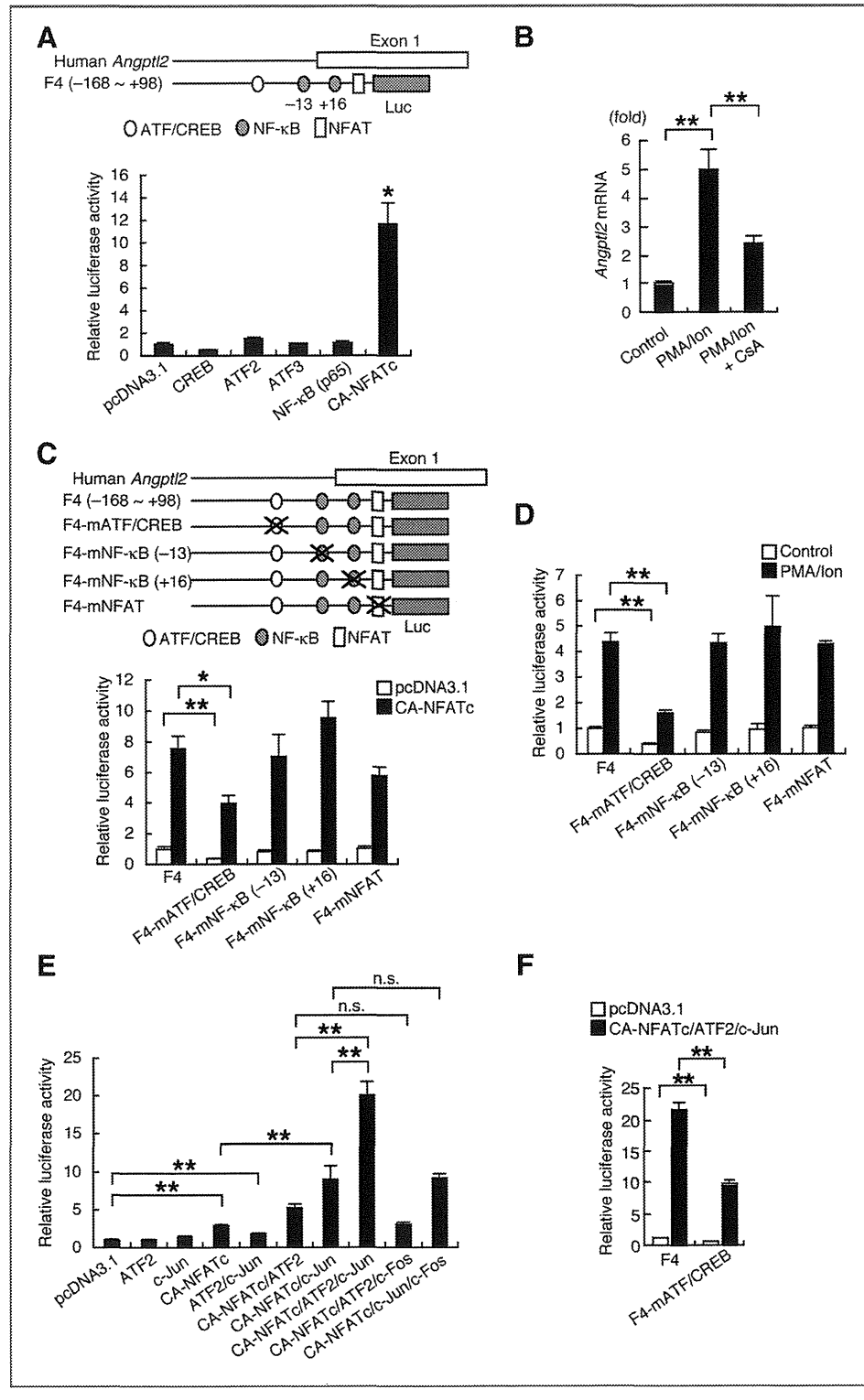

Figure 2. NFATc, ATF2, and c-Jun induce *Angptl2* expression. A, top, schematic diagram of the F4 construct and locations of putative transcription factor–binding sites. The white circle, gray circles, and white box indicate putative ATF/CREB site, NF-κB sites, and NFAT sites, respectively. Luc, luciferase. Bottom, comparison of relative luciferase activity among H460 cells cotransfected with the F4 construct plus CREB, ATF2, ATF3, NF-κB (p65), or CA-NFATc expression plasmids. Reporter activity of cells cotransfected with pcDNA3.1 was set at 1. B, relative *Angptl2* mRNA levels in H460 cells treated with PMA and ionomycin (PMA/Ion) with or without cyclosporin A (CsA). Levels in untreated cells (controls) were set at 1. C, top, schematic diagram of wild-type and mutant F4 constructs. Bottom, comparison of relative luciferase activity among H460 cells cotransfected with wild-type or mutant F4 constructs plus pcDNA3.1 or CA-NFATc expression plasmids. Reporter activity of cells cotransfected with wild-type F4 and pcDNA3.1 was set at 1. D, comparison of relative luciferase activity among H460 cells transfected with wild-type or mutant F4 constructs and treated with PMA/Ion. Reporter activity of cells transfected with the wild-type F4 construct but not treated with PMA/Ion was set at 1. E, comparison of relative luciferase activity among H460 cells cotransfected with F4 plus ATF2, c-Jun, CA-NFAT, or c-Fos expression plasmids or with a combination thereof. Reporter activity of cells cotransfected with pcDNA3.1 was set at 1. F, comparison of relative luciferase activity among H460 cells cotransfected with wild-type or mutant F4 constructs plus indicated expression plasmids (pcDNA3.1 or a CA-NFAT/ATF-2/c-Jun combination). Reporter activity of cells cotransfected with wild-type F4 plus pcDNA3.1 was set at 1. All experiments were carried out at least 3 times. Error bars show SEM. *, $P < 0.05$; **, $P < 0.01$; n.s., no statistical difference.

was also significantly suppressed in F4 constructs bearing a mutant compared with a wild-type ATF/CREB site (Fig. 2C). Furthermore, PMA/Ion treatment increased F4 reporter activity, an effect significantly decreased when we used F4 constructs harboring a mutant ATF/CREB site (Fig. 2D). Overall, it could be possible that NFATc forms a complex with AP-1 heterodimers that enhances NFATc-dependent induction of *Angptl2* expression through the ATF/CREB site. To investigate whether ATF family proteins may bind to ATF/CREB site on the *Angptl2* promoter region, we conducted an electrophoretic

mobility shift assay (EMSA) by using radiolabeled synthetic oligoDNA probe containing DNA sequences of ATF/CREB site on the *Angptl2* promoter region (Supplementary Fig. S4C–E). PMA/Ion treatment induced formation of a specific DNA–protein complex (arrowhead in Supplementary Fig. S4C–E), which was inhibited in the presence of unlabeled ATF/CREB competitors (Supplementary Fig. S4C) or by preincubation with an anti-ATF2 antibody (Supplementary Fig. S4D and S4E, lane 4). These findings suggest that ATF2 binds to the *Angptl2* promoter ATF/CREB site. Preincubation with anti-c-Jun antibody reduced DNA–protein complex formation and promoted emergence of a supershifted band (Supplementary Fig. S4E, lane 5, arrow). Preincubation with an anti-NFATc antibody or addition of unlabeled competitor containing the consensus NFATc-binding site partially reduced levels of the DNA–protein complex (Supplementary Fig. S4C and Supplementary Fig. S4E, lane 6). Preincubation with both anti-c-Jun and anti-ATF2 antibodies (Supplementary Fig. S4E, lane 7) or both anti-c-Jun and anti-NFATc antibodies (Supplementary Fig. S4E, lane 8) markedly reduced levels of the DNA–protein complex and the supershifted band. To assay transcription, we cotransfected the F4 construct into H460 cells with expression vectors encoding CA-NFATc, ATF2, c-Jun, c-Fos, or a combination of these vectors and measured luciferase activity (Fig. 2E). Expression of the ATF2/c-Jun combination enhanced *Angptl2* reporter activity relative to controls. CA-NFATc–dependent induction of reporter activity was augmented by c-Jun coexpression. *Angptl2* reporter activity was also markedly increased by coexpression of CA-NFATc/ATF2/c-Jun. However, CA-NFATc/ATF2–dependent or CA-NFATc/c-Jun–dependent induction of reporter activity was not enhanced by c-Fos coexpression. Furthermore, CA-NFATc/ATF2/c-Jun–dependent reporter activity was significantly suppressed when we used an F4 construct containing a mutant ATF/CREB site (Fig. 2F). To determine whether endogenous NFATc, ATF2, and c-Jun bind to the human *Angptl2* promoter, we used chromatin immunoprecipitation (ChIP) assays in H460 cells (Supplementary Fig. S5A). PMA/Ion treatment of cells resulted in increased NFATc and ATF2 binding to the human *Angptl2* promoter region. Previous studies report that c-Jun is highly expressed and activated in NSCLC cell lines (23, 24). c-Jun binding to the human *Angptl2* promoter region was observed in PMA/Ion-untreated H460 cells, whereas that binding level was unchanged in PMA/Ion-treated cells (Supplementary Fig. S5A). Taken together, these observations show that NFATc plays an important role in *Angptl2* induction and that an ATF2/c-Jun complex likely enhances NFATc-dependent *Angptl2* induction through the ATF/CREB site.

NFATc2 knockdown decreases *Angptl2* expression in tumor cells

The NCI-H460-LNM35 (LNM35) line was established by *in vivo* selection as a highly metastatic subline of the human large cell carcinoma of the lung, NCI-H460 (15). We found that that severe immunodeficient Jak3-deficient NOD-SCID (NOJ) mice (25) subcutaneously injected with LNM35 cells showed shortened survival periods due to high frequency metastasis to lung and lymph nodes compared with mice injected with H460 cells (Supplementary Fig. S6). Interestingly, *Angptl2* mRNA is more abundant in cultured LNM35 cells than in H460 cells (Fig. 3A). We found that NFATc1, NFATc2, and NFATc3 increased *Angptl2* promoter activity in the H460 cells (Supplementary Fig. S5B and S5C). *NFATc2* expression in LNM35 cells was significantly higher than that seen in H460 cells, whereas expression of NFATc1, NFATc3, and NFATc4 was equivalent in both lines (Fig. 3B). NFATc2 protein levels were also markedly increased in LNM35 cells, but ATF2 and c-Jun protein levels were equivalent (Fig. 3C). To examine whether NFATc2 is required for *Angptl2* expression in LNM35 cells, we established 2 LNM35 cell lines each stably expressing a different miR RNA interference (RNAi) expression vector designed to knockdown *NFATc2* (LNM35/miNFATc2-1 and LNM35/miNFATc2-2; Fig. 3D). *Angptl2* expression levels in both lines were significantly decreased compared with control cells and comparable with those seen in H460 cells (Fig. 3E). Invasive activity of LNM35/miNFATc2 cells was decreased compared with controls (Supplementary Fig. S7). These observations suggest that NFATc2 is important for *Angptl2* expression and acquisition of tumor invasivity.

Angptl2-expressing tumor cells contribute to increased tumor metastasis

As indicated in Fig. 1 and Supplementary Fig. S2, ANGPTL2-positive tumor cells exhibit higher metastatic capacity than ANGPTL2-negative cells. We therefore generated 2 independent H460 lines constitutively expressing *Angptl2* (H460/Angptl2-1 and -2) and an H460 line expressing a control vector (H460/Cont; Fig. 4A). Although no differences were observed in *in vitro* growth among all 3 lines (Supplementary Fig. S8A), *in vitro* invasive capacity of the 2 H460/Angptl2 lines was significantly greater than that seen in H460/Cont (Fig. 4B). We next analyzed tumor development after subcutaneous injection of either the 3 lines into mice. Despite equivalence in *in vivo* tumor growth observed among the 2 H460/Angptl2 lines and H460/Cont (Supplementary Fig. S8B and S8C), lung metastasis was more severe in mice bearing H460/Angptl2-1 tumors than in H460/Cont controls (Fig. 4C and D). Tumor angiogenesis was also increased in mice bearing H460/Angptl2-1 compared with H460/Cont cells (Supplementary Fig. S8D and S8E), a finding consistent with our recent report (5). Finally, the survival period of mice bearing H460/Angptl2 tumors was significantly shortened compared with H460/Cont mice (Fig. 4E).

Angptl2 increases tumor cell motility by activating Rac

Time-lapse imaging indicated that H460/Angptl2-1 cells are significantly more motile than are H460/Cont cells (Fig. 5A and B, Supplementary Movie S1 and S2). Histologic analysis indicated that H460/Angptl2-1 cells exhibit a polarized morphology associated with motility, as evidenced by formation of actin-rich lamellipodial protrusions and assembly of paxillin-marked focal complexes at the leading edge, whereas H460/Cont cells displayed nonpolarized morphology with uniform distribution of F-actin and paxillin at the cell periphery (Fig. 5C and D). Because activation of Rac1, a Rho family GTPase, at a cell's leading edge is required to form lamellipodial protrusions

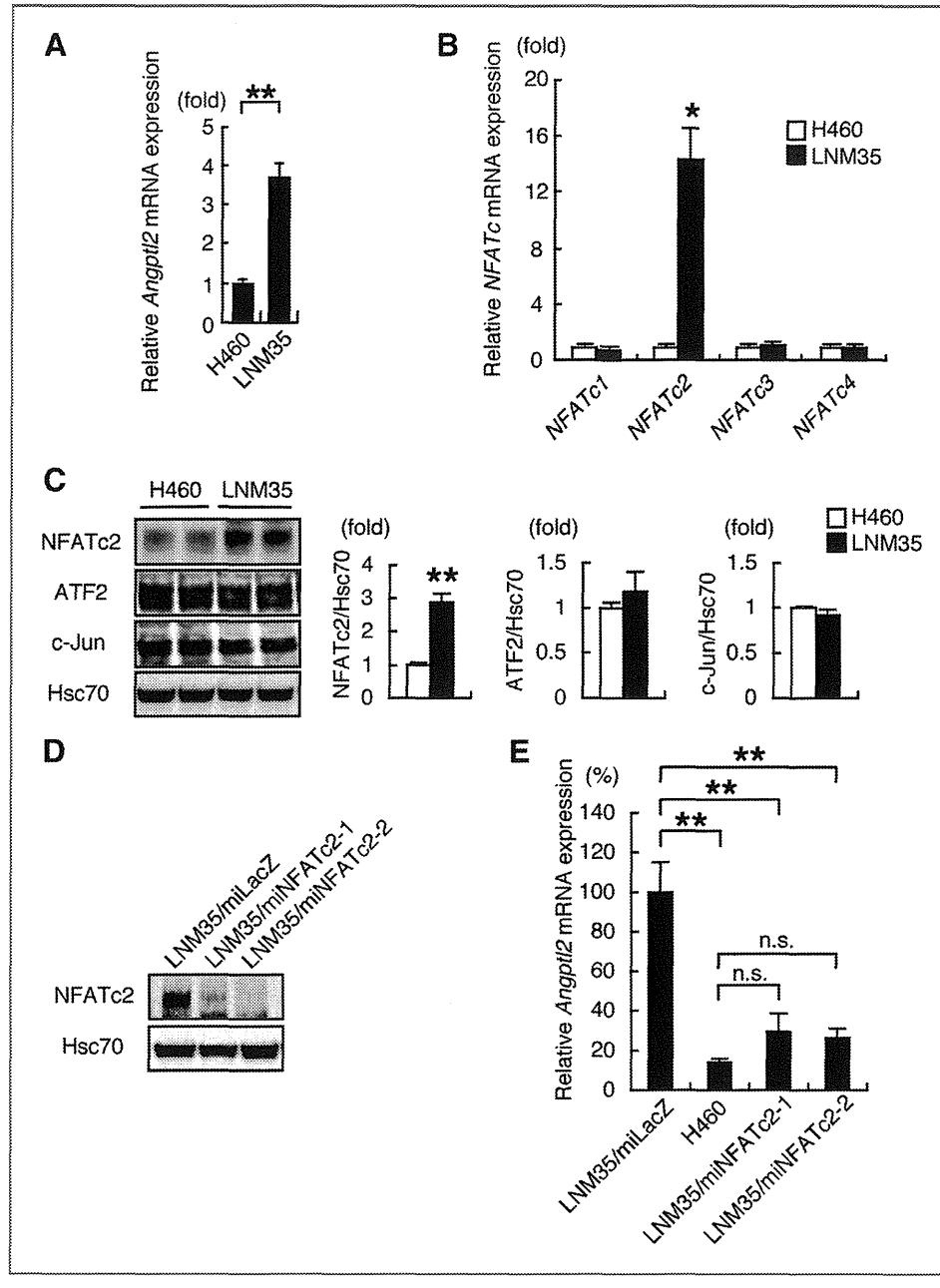

Figure 3. *NFATc2* knockdown decreases *Angptl2* expression. A, comparison of relative *Angptl2* mRNA levels between H460 and LNM35 cells. Data from H460 were set at 1. B, comparison of relative *NFATc* mRNA levels between H460 and LNM35 cells. Data from H460 were set at 1. C, left, representative image of immunoblotting analysis of NFATc2, ATF2, and c-Jun protein levels in H460 and LNM35 cells. Hsc70 served as control. Right, quantitative protein levels of NFATc2, ATF2, and c-Jun relative to Hsc70. Data from H460 were set at 1, respectively. D, representative image of immunoblotting of NFATc2 protein levels in indicated cells. E, comparison of *Angptl2* mRNA levels among indicated cells. Data from LNM35/miLacZ were set to 100%. All experiments were carried out more than 3 times. Error bars show SEM. *, $P < 0.05$; **, $P < 0.01$; n.s., no statistical difference.

required for cell migration (26), we asked whether ANGPTL2 activates Rac1 using a FRET probe to visualize Rac1 activation in H460/Angptl2-1 and H460/Cont cells. Rac1 was potently activated at the leading edge of migrating H460/Angptl2-1 cells, whereas no polarized Rac1 activation was observed in H460/Cont cells (Fig. 5E, Supplementary Movie S3 and S4). Collectively, these data suggest that tumor cell–derived ANGPTL2 promotes actin reorganization and accelerates cell migration via Rac1 in an autocrine and/or paracrine manner.

Angptl2 knockdown suppresses tumor metastasis

Because LNM35 cells express *Angptl2* abundantly and exhibit high metastatic capacity due to enhanced polarized morphology compared with H460 cells (Fig. 3, Supplementary Figs. S6 and S9), we examined the effect of *Angptl2* knockdown in LNM35 cells. Of 4 candidate miR RNAi expression vectors (miAngptl2-a, -b, -c, and -d) recommended by the Invitrogen BLOCK-iT miR RNAi System, miAngptl2-b significantly decreased *Angptl2* expression compared with a LNM35 line harboring *LacZ* knockdown (LNM35/miLacZ) used as a control (Supplementary Fig. S10). We therefore generated 2 independent *Angptl2* knockdown lines: LNM35/miAngptl2-b1 and -b2 (Supplementary Fig. S11A). *In vitro* invasive ability was significantly decreased in both lines compared with LNM35/miLacZ cells, whereas no differences in *in vitro* cell growth were observed among knockdown and control lines (Supplementary

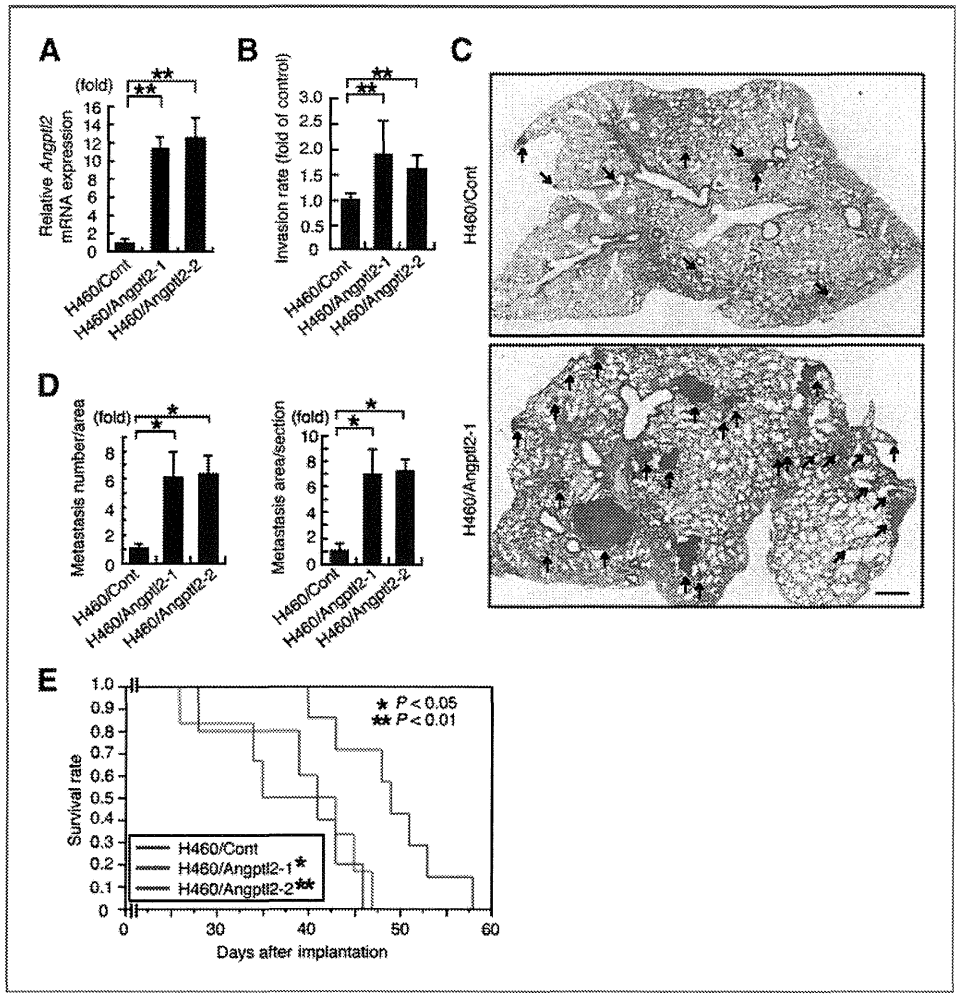

Figure 4. Increased *Angptl2* expression in tumor cells enhances tumor metastasis. A, relative *Angptl2* mRNA levels among indicated cells. Data from H460/Cont were set at 1. B, relative invasive capacity of indicated cells. Data from H460/Cont were set at 1. C, representative hematoxylin and eosin (H&E)-stained images of tumor metastasis (arrows) to lung 4 weeks after injection with H460/Cont (top) or H460/Angptl2-1 (bottom) cells. Scale bar, 200 μm. D, quantitative analysis of (C) for severity of metastasis ($n = 12$). Relative number (left) and area (right) of tumor metastases in lung tissue among indicated cells. Data from H460/Cont were set at 1. E, Kaplan–Meier survival curves of mice bearing tumors derived from H460/Cont . ($n = 10$), H460/Angptl2-1 ($n = 10$), and H460/Angptl2-2 ($n = 7$) cells. All experiments were carried out more than 3 times. Error bars show SD. *, $P < 0.05$; **, $P < 0.01$.

Fig. S11B and S11C). In addition, both knockdown lines displayed less polarized morphology and more uniform distribution of F-actin and paxillin compared with LNM35/miLacZ cells (Supplementary Fig. S12). Mice bearing both *Angptl2* knockdown lines showed no significant difference in tumor growth but exhibited markedly decreased lung metastases compared with mice bearing LNM35/miLacZ cells (Supplementary Fig. S11D–G). Survival times were also extended in mice injected with knockdown versus control lines (Supplementary Fig. S11H). These results suggest that tumor cell–derived ANGPTL2 increases metastasis and that decreased ANGPTL2 expression in tumor cells can attenuate that effect.

Tumor cell–derived ANGPTL2 enhances lung metastasis in mice bearing breast cancer cells

To investigate whether tumor cell–derived ANGPTL2 enhances metastasis in other cancer types, we examined ANGPTL2 expression and function in the human breast cancer lines T47D, MDA-MB453, and MDA-MB231. Only MDA-MB231, which shows an aggressive metastatic phenotype (27), abundantly expressed and secreted ANGPTL2 (Fig. 6A and B). MDA-MB231 cells also expressed NFATc2, ATF2, and c-Jun (Fig. 6A), whereas MDA-MB231 cells stably expressing *NFATc2* RNAi (MB231/miNFATc2) showed significantly decreased *Angptl2* mRNA and protein secretion compared with control MB231/miLacZ cells (Fig. 6C, Supplementary Fig. S13A and S13B). We established 2 independent MDA-MB231 lines expressing miR RNAi (miAngptl2-b) to knockdown *Angptl2* (MB231/miAngptl2-b1 and -2) and a control LacZ RNAi line (MB231/miLacZ). In knockdown lines cellular *Angptl2* mRNA levels and levels of ANGPTL2 protein in the culture medium were significantly decreased compared with those seen in controls (Supplementary Fig. S13C). All 3 lines showed similar *in vitro* growth (Supplementary Fig. S13D), whereas *in vitro* invasive capacity was significantly decreased in knockdown compared with control cells (Supplementary Fig. S13E).

Next, we carried out *in vivo* xenograft tumor experiments by implanting various lines of MDA-MB231 cells into the mouse mammary fat pad. For imaging purposes, we induced a luciferase expression vector into MB231/miAngptl2-b1 and -2 and control MB231/miLacZ cells to create MB231/miAngptl2-b1/luc, MB231/miAngptl2-b2/luc, and MB231/miLacZ/luc, respectively. No difference in *in vivo* tumor growth was seen among the 3 lines (Fig. 6D, Supplementary Fig. S13F). In contrast, lung metastasis was observed in mice bearing MB231/miLacZ/luc 5 weeks after tumor implantation,

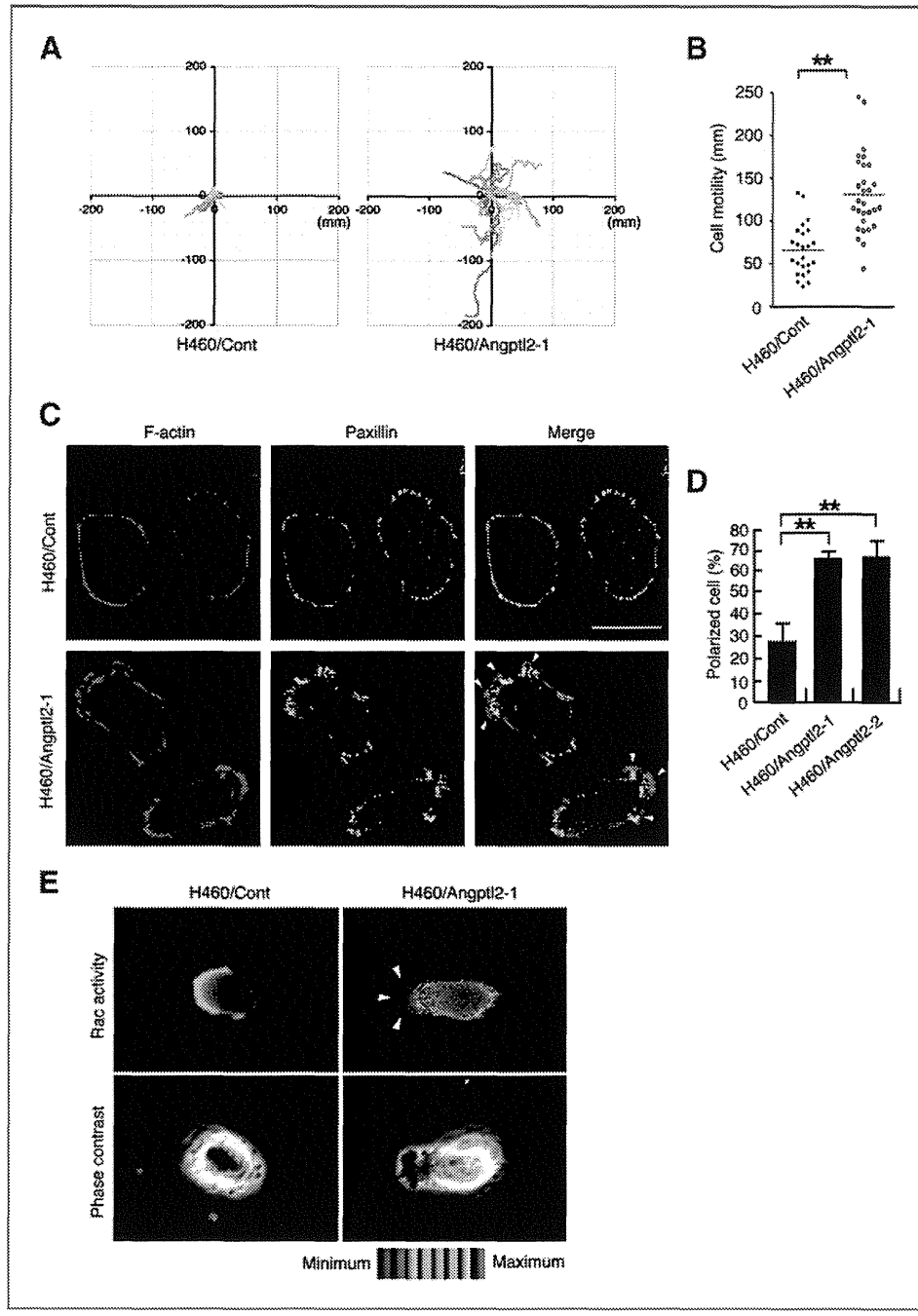

Figure 5. *Angptl2* expression positively correlates with cell motility. A, migration tracks of 20 H460/Cont (left) and H460/Angptl2-1 (right) cells monitored for 5 hours. B, quantitative comparison of the extent of movement of individual tumor cells. C, representative fluorescent immunostaining images for F-actin (left) and paxillin (middle) of H460/Cont (top) and H460/Angptl2-1 (bottom) cells. Arrowheads indicate the leading edge. Scale bar, 20 μm. D, quantitative analysis of polarized cells. E, FRET imaging of Rac activity. Arrowheads indicate site of activated Rac.

whereas fewer metastatic sites at the same time point was observed in mice bearing MB231/miAngptl2-b1/luc. To see equivalent lung metastasis after tumor implantation in mice bearing MB231/miAngptl2-b1/luc required 8 weeks (Fig. 6D). Immunohistochemistry with an anti-CD44 antibody, which detects MDA-MB231 cells (27), showed statistically significant decreases in lung colonization of MB231/miAngptl2-b1 compared with MB231/miLacZ cells (Fig. 6E and F). Moreover, decreased tumor angiogenesis was observed in mice bearing MB231/miAngptl2-b1 compared with MB231/miLacZ cells (Supplementary Fig. S14). Mice bearing the 2 MB231/miAngptl2 lines also showed prolonged survival periods compared with controls (Fig. 6G), suggesting that tumor cell–derived ANGPTL2 accelerates tumor metastasis in breast as well as in lung cancer.

Discussion

Here, we show that tumor cells expressing ANGPTL2 exhibit high metastatic potential through acquisition of invasive and high cell motility phenotypes in an autocrine/paracrine manner. We also showed that NFATc, ATF2, and c-Jun induce

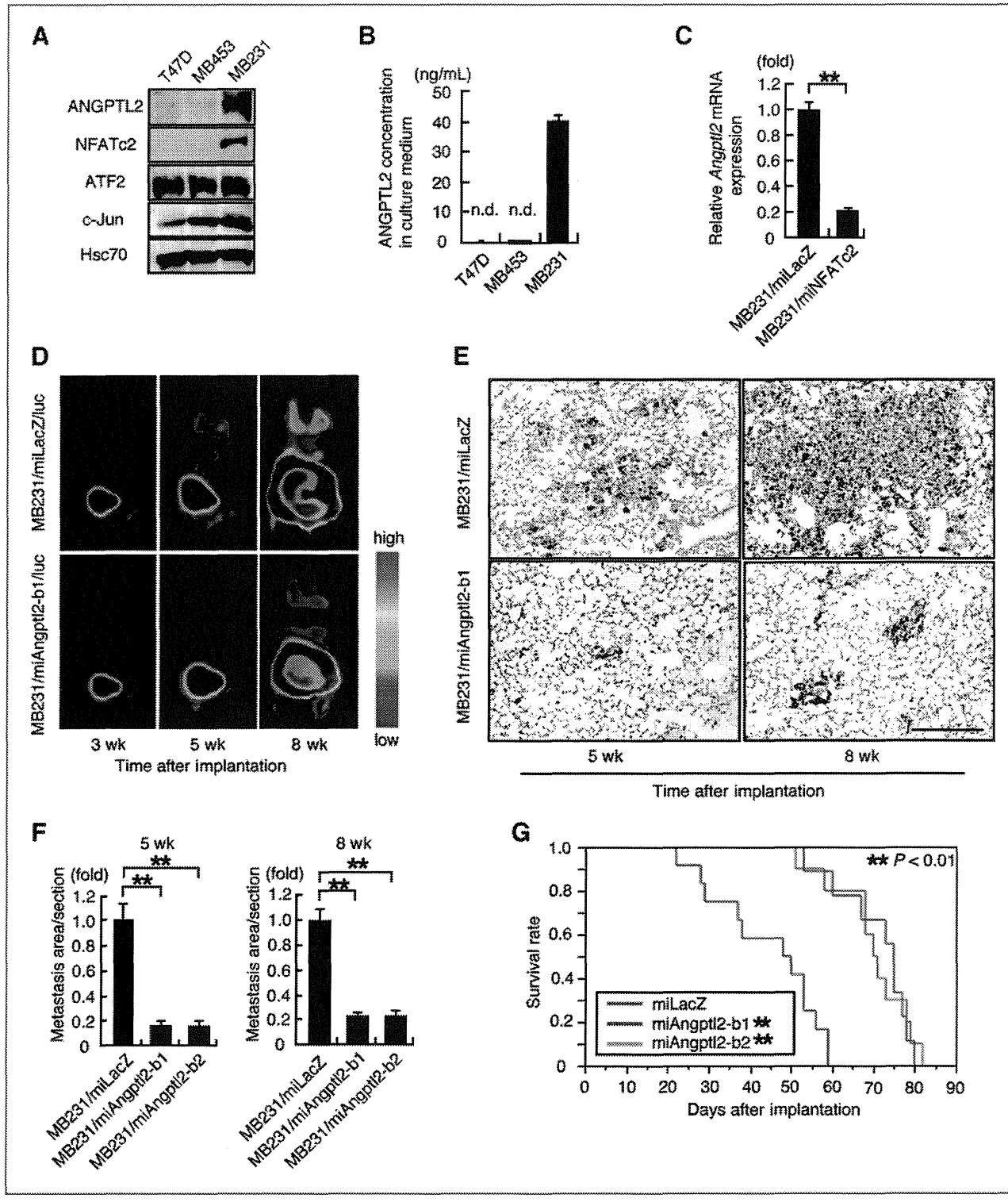

Figure 6. *Angptl2* knockdown in breast cancer cells reduces metastatic capacity. A, representative image of immunoblotting of ANGPTL2, NFATc2, ATF2, and c-Jun protein levels in indicated cells. B, comparison of ANGPTL2 levels in culture medium of indicated cells. n.d., not detected. C, comparison of relative *Angptl2* mRNA levels in indicated cells. Data from MB231/miLacZ were set at 1. D, representative bioluminescence images of mice bearing MB231/miLacZ/luc or MB231/miAngptl2-b1/luc cells. Images were taken at indicated time points after xenografting ($n = 12$). E, representative microscopic images of tumor cells metastasized to lung, as recognized by anti-CD44 immunostaining, 5 (left) and 8 (right) weeks after implantation with MB231/miLacZ (top) or MB231/miAngptl2-b1 (bottom) cells. Scale bar, 500 μm. F, quantitative analysis of (E) for severity of metastasis ($n = 10$). Relative area of tumor metastases in lung among the 3 cell lines at 5 (left) and 8 (right) weeks is shown. Data from MB231/miLacZ were set at 1. G, Kaplan–Meier survival curves of mice bearing tumors derived from MB231/miLacZ ($n = 12$), MB231/miAngptl2-b1 ($n = 10$), or MB231/miAngptl2-b2 ($n = 10$) cells. All experiments were carried out at least 3 times. Error bars show SD. **, $P < 0.01$.

Angptl2 expression, providing a mechanism for tumor cell ANGPTL2 induction. These findings are consistent with previous reports showing that activation of ATF/CREB family proteins and/or the calcineurin/NFATc pathway occurs in aggressively advanced tumors (6, 19, 28, 29).

We have reported that obese adipose tissue–related endoplasmic reticulum (ER) stress increases ANGPTL2 secretion or expression in adipocytes (13). ER stress is easily induced by stresses such as hypoxia, oxidative stress, hypoglycemia, and viral infection, all commonly observed in primary tumor microenvironment (30). We found that *Angptl2* mRNA levels in tumor cells were significantly increased under hypoxia and under nutrition (Supplementary Fig. S15A). In addition, increased ANGPTL2 expression was detected in tumor cells in hypoxic regions (Supplementary Fig. S15B), suggesting that tumor microenvironmental factors, such as hypoxia and/or under nutrition, induce ANGPTL2 expression in tumor cells. Cytoplasmic calcium concentrations increase due to ER stress–dependent calcium release from the ER (31) and activate the serine/threonine phosphatase calcineurin, which in turn dephosphorylates NFATc proteins and triggers their nuclear accumulation (32). NFATc function has been extensively studied in the immune system, but there is increased interest in NFATc activity in cancer (6). We speculate that tumor cell autonomous responses to the microenvironment, such as activation of the ER stress/calcineurin/NFATc pathway and/or ATF/CREB family proteins, induce *Angptl2* expression in tumor cells, resulting in acquisition of aggressively metastatic tumor phenotypes.

Interestingly, a recent report suggests that ANGPTL2 might function in tumor refractoriness to anti-VEGF therapy (33). On the other hand, VEGF reportedly activates an inhibitor of calcineurin/NFATc signaling, namely, the Down syndrome critical region gene 1 (DSCR1; refs. 34, 35). Taken together with these 2 reports, our findings suggest that in tumors refractory to anti-VEGF treatment, suppression of VEGF signaling may inactivate DSCR1 and thereby activate NFATc, resulting in increased ANGPTL2 expression and ANGPTL2-dependent tumor progression. Overall, we propose that the tumor microenvironment activates NFATc and ATF/CREB family proteins in tumor cells, resulting in ANGPTL2 induction and subsequent tumor metastasis.

On the basis of the results of EMSA and ChIP assays, we suggested that NFATc, ATF2, and c-Jun form a complex and bind to the *Angptl2* promoter region in PMA/Ion-treated H460 cells. CA-NFATc–dependent induction of the *Angptl2* reporter activity was augmented by c-Jun coexpression, and the augmentation was significantly enhanced by ATF2 coexpression. In contrast, ATF2 alone did not induce the *Angptl2* reporter activity. Therefore, we consider that ATF2 would be important to form a complex with NFATc and c-Jun to induce the *Angptl2* reporter activity.

We previously reported that ANGPTL2 increases angiogenesis through Rac activation in endothelial cells (13). Consistently, here we found that tumor cell–derived ANGPTL2 increases tumor angiogenesis. Interestingly, we also found that ANGPTL2 directly accelerates tumor cell motility through Rac activation in tumor cells. We observed that EMT occurs prominently in *Angptl2*-expressing human lung cancer cells (Supplementary Figs. S16 and S17) as well as in a chemically induced mouse SCC expressing *Angptl2* (5). Two types of tumor cell movements have been described: a Rac-dependent mesenchymal mode and a Rho-dependent amoeboid mode (36), suggesting that ANGPTL2 induces cell motility in the mesenchymal mode. Because the EMT in tumor cells decreases intercellular adhesion, cell motility is enhanced, resulting in tumor invasion and metastasis. Thus, ANGPTL2 might be a key factor in increasing cell motility in tumor cells with mesenchymal characteristics.

Overall, we show that tumor cell–derived ANGPTL2 accelerates tumor metastasis through increasing tumor cell migration in an autocrine/paracrine manner in addition to enhancing tumor angiogenesis, as described here and reported previously (5; Supplementary Fig. S18). On the basis of these findings, we propose that ANGPTL2 regulates tumor metastasis in human lung and breast cancer. These studies could form the basis of new therapeutic strategies to antagonize tumor metastasis.

Disclosure of Potential Conflicts of Interest

No potential conflicts of interest were disclosed.

Authors' Contributions

Conception and design: M. Endo, M. Nakano, T. Kadomatsu, Y. Oike

Development of methodology: M. Endo, M. Nakano, T. Kadomatsu, K. Miyata, T. Ito, S. Okada, Y. Oike

Acquisition of data (provided animals, acquired and managed patients, provided facilities, etc.): M. Endo, M. Nakano, T. Kadomatsu, S. Fukuhara, H. Kuroda, S. Mikami, T. Hato, J. Aoi, H. Horiguchi, K. Miyata, M. Harada, H. Horio, T. Hishima, H. Nomori, T. Ito, S. Okada, N. Mochizuki, Y. Oike

Analysis and interpretation of data (e.g., statistical analysis, biostatistics, computational analysis): M. Endo, M. Nakano, T. Kadomatsu, S. Fukuhara, H. Kuroda, T. Hato, H. Horiguchi, M. Harada, H. Horio, Y. Oike

Writing, review, and/or revision of the manuscript: M. Endo, M. Nakano, T. Kadomatsu, H. Iwase, Y. Oike

Administrative, technical, or material support (i.e., reporting or organizing data, constructing databases): M. Endo, M. Nakano, T. Kadomatsu, H. Kuroda, T. Hato, H. Odagiri, T. Masuda, Y. Yamamoto, T. Minami, T. Takahashi, H. Iwase, Y. Oike

Study supervision: M. Endo, T. Kadomatsu, H. Odagiri, H. Nomori, S. Okada, Y. Oike

Acknowledgments

The authors thank S. Iwaki, O. Takahashi, and M. Nakata for technical assistance.

Grant Support

This research is funded by the Japan Society for the Promotion of Science (JSPS) through the "Funding Program for World-Leading Innovative R&D on Science and Technology (FIRST Program)" (LS098), initiated by the Council for Science and Technology Policy (CSTP). This work is also supported by Grants-in-Aid for Scientific Research on Priority Areas from the Ministry of Education, Culture, Sports, Science and Technology of Japan and by grants from the Takeda Science Foundation, the Mitsubishi Foundation, and Tokyo Biochemical Research Foundation.

The costs of publication of this article were defrayed in part by the payment of page charges. This article must therefore be hereby marked *advertisement* in accordance with 18 U.S.C. Section 1734 solely to indicate this fact.

Received December 1, 2011; revised February 10, 2012; accepted February 10, 2012; published OnlineFirst February 16, 2012.

Published OnlineFirst February 16, 2012; DOI:10.1158/0008-5472.CAN-11-3878

References

1. Boyle P, Levin B. World Cancer Report 2008. Lyon, France: IARC Press; 2008.
2. Chiang AC, Massague J. Molecular basis of metastasis. N Engl J Med 2008;359:2814–23.
3. Christofori G. New signals from the invasive front. Nature 2006;441: 444–50.
4. Grivennikov SI, Greten FR, Karin M. Immunity, inflammation, and cancer. Cell 2010;140:883–99.
5. Aoi J, Endo M, Kadomatsu T, Miyata K, Nakano M, Horiguchi H, et al. Angiopoietin-like protein 2 is an important facilitator of inflammatory carcinogenesis and metastasis. Cancer Res 2011;71:7502–12.
6. Mancini M, Toker A. NFAT proteins: emerging roles in cancer progression. Nat Rev Cancer 2009;9:810–20.
7. Muller MR, Rao A. NFAT, immunity and cancer: a transcription factor comes of age. Nat Rev Immunol 2010;10:645–56.
8. Flockhart RJ, Armstrong JL, Reynolds NJ, Lovat PE. NFAT signalling is a novel target of oncogenic BRAF in metastatic melanoma. Br J Cancer 2009;101:1448–55.
9. Koenig A, Linhart T, Schlengemann K, Reutlinger K, Wegele J, Adler G, et al. NFAT-induced histone acetylation relay switch promotes c-Myc-dependent growth in pancreatic cancer cells. Gastroenterology 2010;138:1189–99 e1–2.
10. Yoeli-Lerner M, Yiu GK, Rabinovitz I, Erhardt P, Jauliac S, Toker A. Akt blocks breast cancer cell motility and invasion through the transcription factor NFAT. Mol Cell 2005;20:539–50.
11. Zhang H, Xie X, Zhu X, Zhu J, Hao C, Lu Q, et al. Stimulatory cross-talk between NFAT3 and estrogen receptor in breast cancer cells. J Biol Chem 2005;280:43188–97.
12. Okada T, Tsukano H, Endo M, Tabata M, Miyata K, Kadomatsu T, et al. Synoviocyte-derived angiopoietin-like protein 2 contributes to synovial chronic inflammation in rheumatoid arthritis. Am J Pathol 2010; 176:2309–19.
13. Tabata M, Kadomatsu T, Fukuhara S, Miyata K, Ito Y, Endo M, et al. Angiopoietin-like protein 2 promotes chronic adipose tissue inflammation and obesity-related systemic insulin resistance. Cell Metab 2009;10:178–88.
14. Fukuhara S, Sako K, Minami T, Noda K, Kim HZ, Kodama T, et al. Differential function of Tie2 at cell-cell contacts and cell-substratum contacts regulated by angiopoietin-1. Nat Cell Biol 2008;10:513–26.
15. Kozaki K, Miyaishi O, Tsukamoto T, Tatematsu Y, Hida T, Takahashi T, et al. Establishment and characterization of a human lung cancer cell line NCI-H460-LNM35 with consistent lymphogenous metastasis via both subcutaneous and orthotopic propagation. Cancer Res 2000; 60:2535–40.
16. Jauliac S, Lopez-Rodriguez C, Shaw LM, Brown LF, Rao A, Toker A. The role of NFAT transcription factors in integrin-mediated carcinoma invasion. Nat Cell Biol 2002;4:540–4.
17. Yiu GK, Toker A. NFAT induces breast cancer cell invasion by promoting the induction of cyclooxygenase-2. J Biol Chem 2006;281: 12210–7.
18. Chinenov Y, Kerppola TK. Close encounters of many kinds: Fos-Jun interactions that mediate transcription regulatory specificity. Oncogene 2001;20:2438–52.
19. van Dam H, Castellazzi M. Distinct roles of Jun : Fos and Jun : ATF dimers in oncogenesis. Oncogene 2001;20:2453–64.
20. Chen L, Glover JN, Hogan PG, Rao A, Harrison SC. Structure of the DNA-binding domains from NFAT, Fos and Jun bound specifically to DNA. Nature 1998;392:42–8.
21. Macian F, Lopez-Rodriguez C, Rao A. Partners in transcription: NFAT and AP-1. Oncogene 2001;20:2476–89.
22. Ramirez-Carrozzi V, Kerppola T. Asymmetric recognition of nonconsensus AP-1 sites by Fos-Jun and Jun-Jun influences transcriptional cooperativity with NFAT1. Mol Cell Biol 2003;23:1737–49.
23. Szabo E, Riffe ME, Steinberg SM, Birrer MJ, Linnoila RI. Altered cJUN expression: an early event in human lung carcinogenesis. Cancer Res 1996;56:305–15.
24. Shimizu Y, Kinoshita I, Kikuchi J, Yamazaki K, Nishimura M, Birrer MJ, et al. Growth inhibition of non-small cell lung cancer cells by AP-1 blockade using a cJun dominant-negative mutant. Br J Cancer 2008; 98:915–22.
25. Okada S, Harada H, Ito T, Saito T, Suzu S. Early development of human hematopoietic and acquired immune systems in new born NOD/Scid/Jak3null mice intrahepatic engrafted with cord blood-derived CD34 + cells. Int J Hematol 2008;88:476–82.
26. Waterman-Storer CM, Worthylake RA, Liu BP, Burridge K, Salmon ED. Microtubule growth activates Rac1 to promote lamellipodial protrusion in fibroblasts. Nat Cell Biol 1999;1:45–50.
27. Kao J, Salari K, Bocanegra M, Choi YL, Girard L, Gandhi J, et al. Molecular profiling of breast cancer cell lines defines relevant tumor models and provides a resource for cancer gene discovery. PLoS One 2009;4:e6146.
28. Lopez-Bergami P, Lau E, Ronai Z. Emerging roles of ATF2 and the dynamic AP1 network in cancer. Nat Rev Cancer 2010;10: 65–76.
29. Vlahopoulos SA, Logotheti S, Mikas D, Giarika A, Gorgoulis V, Zoumpourlis V. The role of ATF-2 in oncogenesis. Bioessays 2008;30: 314–27.
30. Moenner M, Pluquet O, Bouchecareilh M, Chevet E. Integrated endoplasmic reticulum stress responses in cancer. Cancer Res 2007;67: 10631–4.
31. Xu C, Bailly-Maitre B, Reed JC. Endoplasmic reticulum stress: cell life and death decisions. J Clin Invest 2005;115:2656–64.
32. Crabtree GR, Olson EN. NFAT signaling: choreographing the social lives of cells. Cell 2002;109 Suppl: S67–79.
33. Crawford Y, Kasman I, Yu L, Zhong C, Wu X, Modrusan Z, et al. PDGF-C mediates the angiogenic and tumorigenic properties of fibroblasts associated with tumors refractory to anti-VEGF treatment. Cancer Cell 2009;15:21–34.
34. Minami T, Horiuchi K, Miura M, Abid MR, Takabe W, Noguchi N, et al. Vascular endothelial growth factor- and thrombin-induced termination factor, Down syndrome critical region-1, attenuates endothelial cell proliferation and angiogenesis. J Biol Chem 2004; 279:50537–54.
35. Minami T, Yano K, Miura M, Kobayashi M, Suehiro J, Reid PC, et al. The Down syndrome critical region gene 1 short variant promoters direct vascular bed-specific gene expression during inflammation in mice. J Clin Invest 2009;119:2257–70.
36. Sanz-Moreno V, Gadea G, Ahn J, Paterson H, Marra P, Pinner S, et al. Rac activation and inactivation control plasticity of tumor cell movement. Cell 2008;135:510–23.

Fenton Reaction Induced Cancer in Wild Type Rats Recapitulates Genomic Alterations Observed in Human Cancer

Shinya Akatsuka[1], Yoriko Yamashita[1], Hiroki Ohara[1], Yu-Ting Liu[2], Masashi Izumiya[3], Koichiro Abe[3,4], Masako Ochiai[3], Li Jiang[1], Hirotaka Nagai[1,2], Yasumasa Okazaki[1], Hideki Murakami[5], Yoshitaka Sekido[5], Eri Arai[6], Yae Kanai[6], Okio Hino[7], Takashi Takahashi[8], Hitoshi Nakagama[3], Shinya Toyokuni[1]*

1 Departments of Pathology and Biological Responses, Nagoya University Graduate School of Medicine, Showa-ku, Nagoya, Japan, **2** Department of Pathology and Biology of Diseases, Kyoto University Graduate School of Medicine, Sakyo-ku, Kyoto, Japan, **3** Division of Cancer Development System, National Cancer Center Research Institute, Chuo-ku, Tokyo, Japan, **4** Department of Internal Medicine, Teikyo University School of Medicine, Itabashi-ku, Tokyo, Japan, **5** Division of Molecular Oncology, Aichi Cancer Center Research Institute, Chikusa-Ku, Nagoya, Japan, **6** Division of Molecular Pathology, National Cancer Center Research Institute, Chuo-ku, Tokyo, Japan, **7** Department of Pathology and Oncology, Juntendo University School of Medicine, Bunkyo-ku, Tokyo, Japan, **8** Molecular Carcinogenesis, Nagoya University Graduate School of Medicine, Showa-ku, Nagoya, Japan

Abstract

Iron overload has been associated with carcinogenesis in humans. Intraperitoneal administration of ferric nitrilotriacetate initiates a Fenton reaction in renal proximal tubules of rodents that ultimately leads to a high incidence of renal cell carcinoma (RCC) after repeated treatments. We performed high-resolution microarray comparative genomic hybridization to identify characteristics in the genomic profiles of this oxidative stress-induced rat RCCs. The results revealed extensive large-scale genomic alterations with a preference for deletions. Deletions and amplifications were numerous and sometimes fragmented, demonstrating that a Fenton reaction is a cause of such genomic alterations *in vivo*. Frequency plotting indicated that two of the most commonly altered loci corresponded to a *Cdkn2a/2b* deletion and a *Met* amplification. Tumor sizes were proportionally associated with *Met* expression and/or amplification, and clustering analysis confirmed our results. Furthermore, we developed a procedure to compare whole genomic patterns of the copy number alterations among different species based on chromosomal syntenic relationship. Patterns of the rat RCCs showed the strongest similarity to the human RCCs among five types of human cancers, followed by human malignant mesothelioma, an iron overload-associated cancer. Therefore, an iron-dependent Fenton chemical reaction causes large-scale genomic alterations during carcinogenesis, which may result in distinct genomic profiles. Based on the characteristics of extensive genome alterations in human cancer, our results suggest that this chemical reaction may play a major role during human carcinogenesis.

Citation: Akatsuka S, Yamashita Y, Ohara H, Liu Y-T, Izumiya M, et al. (2012) Fenton Reaction Induced Cancer in Wild Type Rats Recapitulates Genomic Alterations Observed in Human Cancer. PLoS ONE 7(8): e43403. doi:10.1371/journal.pone.0043403

Editor: Kamaleshwar Singh, Texas Tech University, United States of America

Received March 2, 2012; **Accepted** July 19, 2012; **Published** August 29, 2012

Funding: This study was supported by Princess Takamatsu Cancer Research Fund (10-24213); a Grant-in-Aid for Cancer Research from the Ministry of Health, Labour and Welfare of Japan; and a Grant-in Aid from the Ministry of Education, Culture, Sports, Science and Technology of Japan. The funders had no role in study design, data collection and analysis, decision to publish, or preparation of the manuscript.

Competing Interests: The authors have declared that no competing interests exist.

* E-mail: toyokuni@med.nagoya-u.ac.jp

Introduction

Cancer is a disease of accumulated genomic alterations, presumably caused by a systematic process during cellular injury and repair. Causative agents for carcinogenesis are numerous including γ-radiation, ultraviolet radiation, inflammation, chemicals and iron overload [1]. Genomic data of a variety of human cancers is currently analyzed either with array-based comparative genomic hybridization (CGH) [2] or next-generation sequencing [3,4]. These projects are performed to find causative gene mutations that will lead to identifying novel chemicals or antibodies directed for the interactions of responsible signaling molecules. These efforts are expected to result in developments of effective drugs. However, cancer prevention in daily life is as important as its therapy.

In the present study, we sought to resolve roles of iron-mediated oxidative stress during carcinogenesis using array-based CGH. Oxidative stress is constitutively caused by the metabolism of molecular oxygen [5], but is mainly regulated by various antioxidant systems. However, in a variety of pathological conditions, oxidative stress loads exceed the antioxidant capacity [6]. Iron is the most abundant heavy metal in mammals, such as rodents and humans. Whereas iron is essential for oxygen transport as a component of hemoglobin, excess iron has been associated with carcinogenesis [7,8], presumably through a Fenton reaction [9]. Ionic forms of iron are barely soluble at a neutral pH, but ferric nitrilotriacetate (Fe-NTA), an iron chelate, is soluble at pH 7.4 and is an efficient catalytic agent for the Fenton reaction [10]. In the 1980s, our group established that repeated intraperitoneal administrations of Fe-NTA induce a high incidence of renal cell carcinoma (RCC) in rodents [11,12]. Later, we

showed that the renal injury occurs through a Fenton reaction with a variety of hydroxyl radical-mediated chemical products, such as 8-hydroxy-2′-deoxyguanosine [13,14] and 4-hydroxy-nonenal [15,16]. It is established that an iron overload in many pathological conditions is associated with the presence of catalytic iron [17,18].

Accordingly, by evaluating whole genome of RCCs, we could find a general principle for the genomic alterations under oxidatively-stressed conditions. We reported a *Cdkn2a/2b* deletion using microsatellite analysis in this model [19]. In this study, we evaluated the whole genome of Fe-NTA-induced rat RCCs and their cell lines using array-based CGHs. Furthermore, we transformed the data into a human genome through chromosomal syntenic relationship and analyzed the association.

Results

Genome-wide Views of DNA Copy Number Alterations in Fe-NTA-induced Rat RCCs

Fifteen rat RCC DNA samples, which included 13 primary tumor samples and 2 cell line samples, were hybridized on Agilent oligonucleotide microarrays for CGH with 181,978 genomic loci (GEO accession: GSE36101). Comparing different array-based CGH profiles in a quantitative manner is difficult. A shift in the mean copy number is caused by polyploidy and the contamination of normal cells. Therefore, we have developed a statistical method that considers these factors to estimate the chromosomal copy number (**Methods S1**). In this paper, array-based CGH profile data analyses are based on the estimated copy numbers using this method.

Array-based CGH profiling revealed that genomes of the Fe-NTA-induced rat RCCs are often complex and have many extensive chromosomal alterations (**Figs. 1A and S1**). A whole genome frequency analysis with 15 samples identified recurrent regions of a copy number aberration in the Fe-NTA-induced RCCs (**Fig. 1B**). Copy number aberrations were determined based on the distribution of the log2 ratio values that were recalculated with the estimated copy number for a set of 13 primary tumors and 2 cell lines (**Fig. S2**). In this distribution, the thresholds that represented gain and loss were chosen at ± 0.377. A threshold representing amplification was chosen at +0.811 whereas a homozygous deletion (complete loss) was assigned to the position at which the copy number was estimated as 0. The most characteristic global feature uncovered by the frequency analysis was a predisposition to lose an extensively wide region of chromosomes, especially for chromosomes 3, 5, 6, 8, 9, 14, 15, 17 and 20. The second feature was a frequent amplification over a long pericentromeric region in chromosome 4.

Frequent Chromosomal Loss in Rat Chromosome 5 and Homozygous Deletion at the *Cdkn2a/2b* Locus

Chromosome 5 underwent an extensive loss in copy number, not less than that in other chromosomes (e.g., chromosomes 6, 8 and 20) (**Fig. 1B**). As it relates to extensive loss, homozygous deletions were most frequently observed at the *Cdkn2a/2b* locus on chromosome 5 (**Fig. 2A**). This commonly deleted region included two loci (*Cdkn2a* and *Cdkn2b*) for three distinct tumor suppressor genes (*p16* and *p19* in *Cdkn2a*; *p15* in *Cdkn2b*) (**Fig. 2B**). Shutdown of *p16/p19* and *p15* mRNA expression was confirmed in the samples that contained a homozygous deletion at the *Cdkn2a/2b* locus (**Figs. 2C and 2D**). In samples with a hemizygous deletion at the *Cdkn2a* locus (i.e., FB32-4, FB28-7), *p16* and *p19* expressions were downregulated, presumably because the promoter regions of the remaining alleles were methylated. However, some of the samples with either a hemizygous or no deletion (e.g., FB14-3; BF51-1; FB14-6; FB30-5 and FB33-7) showed a marked over-expression of *p16* and *p19*.

Frequent Amplifications Over the Pericentromeric Region of Chromosome 4 and Amplification at the *Met* Locus

Over a long portion of the pericentromeric region in chromosome 4, frequent copy number gain and amplification were observed (**Fig. 1B**). Genomic amplification and gene expression in the corresponding areas of chromosome 4 were mostly proportional (**Fig. S3**). A bar plot of the amplified region along the pericentromeric region in chromosome 4 revealed that *Met* oncogene resides in the most common overlapping genomic section (**Fig. 3A**). The most overlapping section with a length of approximately 222 kb consisted of an amplified region in 11/15 samples and contained only one RefSeq-curated gene (*Met*) (**Fig. 3B**). A greater than 5-fold increase in *Met* mRNA expression was observed in 6 samples among the 9 tumors that contained a genomic amplification of *Met* (**Fig. 3C**).

Collectively, regarding chromosomal aberrations at these two cancer-related loci, every examined carcinoma including the two cell lines contained either the *Met* amplification or the *Cdkn2a/2b* deletion (**Table 1, Figs. 2B and 3B**). Other common genetic alterations are summarized in **Table S1** (20 deleted genes, common in 2–4 RCC tumors) and **Table S2** (340 amplified genes, common in 2–9 RCC tumors). Among those *Zbtb38* amplification was confirmed for overexpression (**Fig. S4**).

Tumor Size of Fe-NTA-induced RCCs is Regulated by Genetic Features

We examined the associations between genetic alterations and various RCC traits including those summarized in **Table 1**. Among all of the relationships examined, *Met* expression and tumor size were proportionally associated (**Fig. 4A**). Furthermore, a hierarchical clustering of tumors based on whole patterns of chromosomal changes revealed that a group of large tumors (i.e., FB7-7, FB30-5 and FB33-7) corresponded to a distinct cluster (**Fig. 4B**). Therefore, a tumor trait, size at the time the tumor was clinically overt, was associated with the entire array-based CGH profiles.

Comparison of Copy Number Alteration Profiles in Cancer Genomes Between Rats and Humans

To determine the general principle of large-scale genomic changes in cancer across mammalian species, we compared cancer genomes of rats and humans as a whole spectrum of chromosomal alterations. First, we transformed the rat array-based CGH profiles onto human chromosomes according to a synteny between the two species. Thereafter, we compared the whole patterns based on estimated copy numbers using multidimensional data analysis methods. We found that Fe-NTA-induced rat RCC was most similar to human RCCs, followed by human malignant mesothelioma (**Figs. 5A and 5B**).

Discussion

In this study, we report for the first time analyses of the entire data from array-based CGH applied to a Fenton chemistry-induced carcinogenesis in a rat kidney model [20]. We found that oxidative stress causes extensive genomic alterations in the induced cancer genome at chromosomal level (**Fig. 1A**). It is well known that a majority of human malignant solid tumors possess gains or losses in numerous chromosomes [21,22], and amplification can

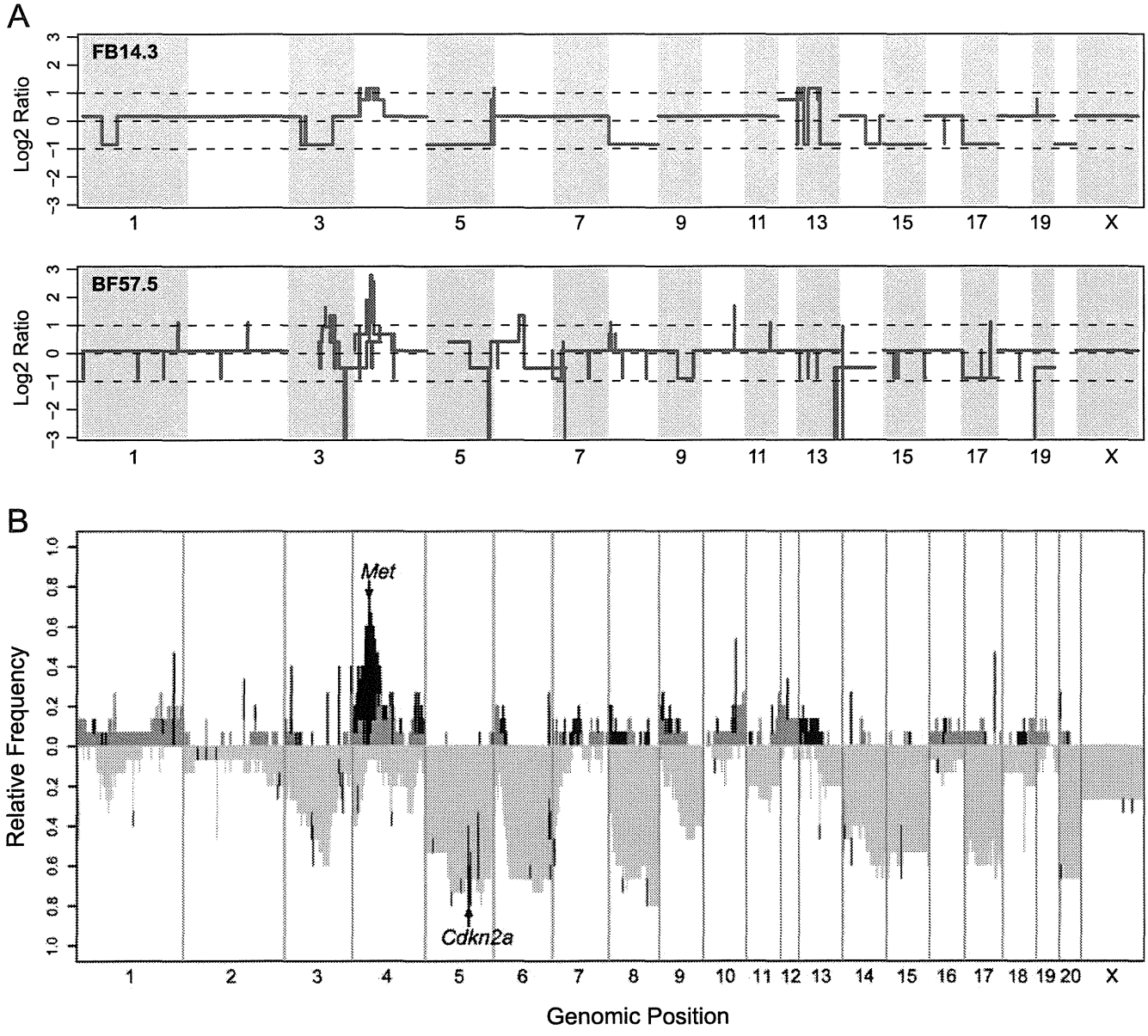

Figure 1. Genome-wide views of DNA copy number alterations in Fe-NTA induced rat renal cell carcinomas (RCCs). (A) Representative array-based CGH profiles from two RCC tumors. The red lines show log2 ratios of the estimated copy number over the inferred cancer ploidy versus the genomic position for all of the CGH microarray probes. (B) Frequency distribution of copy number aberrations across the whole rat genome. The relative frequencies of amplification (dark red), gain (tomato), loss (green yellow) and homozygous deletion (dark green) within 13 RCC tumors and two RCC cell lines are plotted at each genomic position. Two cancer-related loci, *Met* and *Cdkn2a*, which were most frequently affected by copy number aberration are indicated by the arrows.
doi:10.1371/journal.pone.0043403.g001

be a suitable target for cancer chemotherapy. During the carcinogenic process of such tumors, chromosomal instability is thought to contribute as a driving factor [23]. Among wild-type rodent carcinogenesis models, however, few models report using primary tumor samples extensive genetic alterations because of chromosomal instability [24,25]. Radiation-induced murine malignant lymphoma [26] and murine lung adenocarcinoma induced by 4-(methylnitrosamino)-1-(3-pyridyl)-1-butanone, a carcinogen present in tobacco smoke [27], revealed slightly more gross chromosomal aberrations than the corresponding spontaneous tumors, albeit the low resolution in the report (bacterial artificial chromosome [BAC] array of ~6,500). The facts that control rats exhibit no RCCs [11,12] and Fe-NTA-induced rat RCC model exhibits an equivalence to human cancers in genomic alterations at chromosomal level strongly support the idea that this carcinogenesis model mimics an actual carcinogenic process in those humans who lack strong cancer susceptibility traits.

Conversely, mice with multiple genetically-engineered cancer-associated genes show genetic alteration of this kind [28]. We think that those experiments correspond to an established mutator phenotype [29] and, thus, to the carcinogenic process in humans who have strong cancer susceptibility traits such as Li-Fraumeni syndrome (*p53*) [30] or melanoma kindreds (*p16*) [31]. As a hereditary rat RCC model, we also analyzed the RCCs of Eker rats, which do not show aggressive characteristics, such as metastasis [32,33,34]. We observed that these RCCs showed null